

## **Chemosensory modulation of eye-body coordination in larval zebrafish**

Samuel K. H. Sy,<sup>1-6,\*</sup> Danny C. W. Chan,<sup>1-5</sup> Jenny J. Zhang,<sup>1-5</sup> Jing Lyu,<sup>1-5</sup> Crystal Feng,<sup>1-5</sup> Kui Wang,<sup>7</sup> Vincent C. T. Mok,<sup>1-5</sup> Kenneth K. Y. Wong,<sup>6,8</sup> Yu Mu,<sup>7</sup> Owen Randlett,<sup>9</sup> Yu Hu,<sup>10</sup> Ho Ko<sup>1-5,\*</sup>

### **Affiliations**

<sup>1</sup>Division of Neurology, Department of Medicine and Therapeutics, Faculty of Medicine, The Chinese University of Hong Kong, Shatin, New Territories, Hong Kong SAR, China.

<sup>2</sup>Li Ka Shing Institute of Health Sciences, Faculty of Medicine, The Chinese University of Hong Kong, Shatin, New Territories, Hong Kong SAR, China.

<sup>3</sup>Margaret K. L. Cheung Research Centre for Management of Parkinsonism, Faculty of Medicine, The Chinese University of Hong Kong, Shatin, New Territories, Hong Kong SAR, China.

<sup>4</sup>Lau Tat-chuen Research Centre of Brain Degenerative Diseases in Chinese, Faculty of Medicine, The Chinese University of Hong Kong, Shatin, New Territories, Hong Kong SAR, China.

<sup>5</sup>Gerald Choa Neuroscience Institute, The Chinese University of Hong Kong, Shatin, New Territories, Hong Kong SAR, China.

<sup>6</sup>Advanced Biomedical Instrumentation Centre, Hong Kong Science Park, Pak Shek Kok, New Territories, Hong Kong SAR, China.

<sup>7</sup>Institute of Neuroscience, Chinese Academy of Sciences, Shanghai, China.

<sup>8</sup>Department of Electrical and Electronic Engineering, Faculty of Engineering, The University of Hong Kong, Pok Fu Lam, Hong Kong Island, Hong Kong SAR, China.

<sup>9</sup>Institut national de la santé et de la recherche médicale, Université Claude Bernard Lyon 1, Lyon, France.

<sup>10</sup>Department of Mathematics and Division of Life Science, Faculty of Science, Hong Kong University of Science and Technology, Clear Water Bay, New Territories, Hong Kong SAR, China.

\*Correspondence: S.K.H.S. ([khsamuelsy@gmail.com](mailto:khsamuelsy@gmail.com)) or H.K. ([ho.ko@cuhk.edu.hk](mailto:ho.ko@cuhk.edu.hk))

## Abstract

Coordinated eye-body movements are essential for many animal behaviors, yet the influence of chemosensory inputs on these movements remains underexplored. Here, we enhance the Fish-On-Chips optofluidic platform to reveal that larval zebrafish use coupled saccade-tail flips for chemosensory avoidance, but not pursuit. Spontaneous saccades, which alternate in direction, are closely synchronized with tail flips via anticipatory adjustments in tail flip event rate, directionality, and kinematics. In response to ethologically representative chemosensory cues, this coordination is differentially modulated based on valence. Aversive chemical cues increase saccade frequency and the proportion of saccade-coupled tail flips, while also enhancing the turning intent as the coupling strengthens. Conversely, appetitive chemicals promote more sustained gliding movements without impacting saccades or their tail flip coupling. Brain-wide neuronal activity imaging reveals that the pallium, a cortical homolog in teleosts, strongly represents the sensorimotor transformation of aversive cue-associated coupled saccade-tail flips. Our findings underscore the critical role of chemosensory cues in regulating eye-body coordination in an early vertebrate species, highlighting a deep evolutionary integration of sensory inputs to optimize locomotion.

## Introduction

Eye-body coordination underpins a wide range of visuomotor behaviors across the animal kingdom, from bird flight and octopus feeding to fish hunting and human calligraphy<sup>1–4</sup>. Each species has evolved unique adaptations to optimize these behaviors within their specific ecological contexts. In many animals including humans, quick and synchronous movements of both eyes in the same direction, known as conjugate saccades (hereafter referred to as saccades), aid gaze control during locomotion and body orientation changes<sup>5–9</sup>. This coordination allows us to track moving objects, maintain visual fixation, and navigate our environments effectively. In Parkinson's disease patients, saccade dysfunction is associated with turning difficulties<sup>10</sup>. Naturally, visual and mechanosensory cues are the principal regulators of visuomotor behaviors, providing the sensory feedback necessary for adjusting movements in real-time<sup>11–18</sup>. When exploring an environment, however, an animal must perform multisensory integration to optimize decision making and motor program selection<sup>19–23</sup>.

In pursuit and avoidance behaviors, chemosensation plays a pivotal role by modulating heading direction and locomotion based on innate and/or learnt valence values<sup>24–37</sup>. This sensory modality provides critical information about the chemical makeup of the environment, which can signal the presence of food<sup>25</sup>, predators<sup>26,27</sup>, or mates<sup>27,28</sup>. For example, a sudden surge of noxious chemical signals can trigger fleeing. Concurrently, both independently and in coordination with body motions, eye movements continuously influence visual input and locomotion<sup>6,38</sup>. In addition, chemical cues may trigger arousal state changes, leading to more frequent visual scanning and heightened alertness<sup>39</sup>. Dynamic interactions between sensory and motor systems ensure that multimodal cues are integrated seamlessly, allowing for precise and timely responses. Unraveling the relationship between chemosensation, eye movements, and locomotion has significant implications for our understanding of behavioral control in animals.

In this study, we investigated whether chemosensation modulates the coordination of eye and body movements in larval zebrafish, which are optically transparent and lack a flexible neck<sup>40,41</sup>. These characteristics facilitate brainwide neuronal imaging<sup>42</sup> and simplify the analysis of eye-body coordination, making them an ideal vertebrate model organism. Recognizing the potential complexities of the interplay between chemosensation and motor outputs, and that of the saccade-body movement relationship in visuomotor behaviors, we hypothesized that chemosensory cues could trigger a coordinated behavioral response in larval zebrafish. Specifically, we postulated that saccades and tail flips are jointly modulated in response to chemical cue valence. To test this hypothesis, we advanced our Fish-on-Chips system<sup>24</sup>, enabling more efficient chemical valence screening and enhanced imaging in behaving larvae. This integrated platform allowed us to simultaneously record body-wide behavioral output and brain-wide neuronal activities in response to chemicals of different valances, providing a unique opportunity to elucidate the neural mechanisms underlying chemosensory control of eye-body movement coordination in larval zebrafish.

We revealed that temporally coupled saccade-body turns are characterized by a larger tail flip directional bias, and exhibit directional alignment and temporal coordination with both anticipatory and subsequent tail flips. In contrast, these characteristics are not observed in saccade-independent forward swims. Upon exposure to chemosensory stimuli, saccade-tail flip coordination is enhanced by aversive chemicals. This leads to more frequent saccades and saccade-coupled tail flips, as well as a larger turn amplitude with stronger saccade coupling. In comparison, appetitive chemicals drive longer forward swims and do not affect the coordination between saccades and tail flips. Across the brain, we identified valence and motor representations underlying chemosensory input-associated coupled saccade-tail flips, pinpointing the telencephalic pallium as a potential key coordinator. Our findings indicate that in larval zebrafish, chemosensory cues can influence eye-body coordination based on innate perceived valence, serving as an integrated response to achieve locomotive goals.

## Results

### Assessing the valence of ecologically relevant chemicals across concentrations

The innate hedonic responses of zebrafish larvae and other teleosts to various chemicals have remained largely unknown, owing in part to limited reports, as well as the inherently high variability of such responses<sup>43–46</sup>. To address this gap, we developed a fluidics-based quadrant assay (**Figure 1a**, **Supplementary Figure 1a**), as part of the refined Fish-on-Chips platform<sup>24</sup>. Drawing from relevant literature, we first assayed various classes of chemicals or odors that are ecologically significant to zebrafish adults and/or larvae, across three successive orders of concentration for each ( $n = 313$  larvae in 83 group-based assays for 9 chemicals, and included control assays with water in all quadrants) (**Figure 1b**). These included two amino acids, namely valine (Val) and alanine (Ala)<sup>29,30</sup>, the sex pheromone prostaglandin F2α (PGF2α)<sup>28</sup>, putrefaction-associated diamines including cadaverine (Cad) and putrescine (Put)<sup>24,26</sup>, bile acids<sup>32,33</sup> including chenodeoxycholic acid (CDCA) and glycodeoxycholic acid (GDCA), adenosine (Ade) which is a food-associated cue<sup>25</sup>, and sodium chloride (NaCl) which determines salinity<sup>31</sup>.

By analyzing the difference of time spent of the larvae in each quadrant compared with the control quadrant (see **Methods**), we were able to identify the particular chemicals and the concentrations that either attract, repel, or have no discernible effect on larval zebrafish (**Figure 1c**). In control conditions with all quadrants filled with water, the larval zebrafish distribute their time evenly across the four quadrants, indicating no intrinsic bias in the setup (**Figure 1c**). We observed that Val (at 100 µM or above) and Ala (at 10 µM and 1 mM) are attractive to the larvae, similar to the preference seen in adult zebrafish <sup>29,30</sup>. Interestingly, despite being a sex pheromone <sup>28</sup>, PGF2 $\alpha$  is already attractive to the larval zebrafish at a concentration of 1 µM. We also confirmed that Cad and Put, at 10 µM or 100 µM and above, respectively, are repellent <sup>24,26</sup>. CDCA (at 10 µM and above) and GDCA (at 1 µM and above), which are examples of bile acids typically considered as social cues <sup>32,33</sup>, were found to be repellent. For PGF2 $\alpha$  and the bile acids, which require 0.5% DMSO for dissolution, we obtained consistent results comparing data using either water or 0.5% DMSO in the control quadrant (**Supplementary Figures 1b, c**), and therefore pooled the results for analysis (**Figure 1c**).

Notably, larval zebrafish generally respond to attractive and aversive chemicals at the highest concentration tested, with the exception of PGF2 $\alpha$ . Adenosine, known to attract adult zebrafish <sup>25</sup>, did not exhibit any attractant or repellent effects on the larvae. Furthermore, NaCl, a recently reported aversive olfactory stimulus <sup>31</sup>, showed no impacts on the larvae in our assays. Note that however, our assay predominantly presents absolute concentrations of NaCl with minimal gradient, which could be a critical factor as zebrafish may rely on its spatial gradient for navigation to avoid high salinity areas <sup>31</sup>.

In summary, our assay has determined that at suitable concentrations, Val, Ala, and PGF2 $\alpha$  act as attractive chemicals to larval zebrafish, whereas Cad, Put, CDCA, as well as GDCA serve as repellent chemicals.

### An optimized optofluidic setup for recording saccade, tail flip and neuronal activity

Studying eye-body movement coordination under chemosensory cue influence and its neural basis requires a method for precisely controlled chemical delivery. This also necessitates simultaneous recordings of brain-wide neuronal activity and the movements of the eyes and tail, unconfounded by vestibular activation and motions of other body parts. To this end, we enhanced the integrated microfluidic-light sheet imaging setup of the Fish-on-Chip platform <sup>24</sup> for concurrent imaging of both neuronal and behavioral events.

We developed a new setup featuring improved larval subject tethering, enhanced capability for multiple chemical delivery, and optimized imaging of forebrain regions. The design includes offset fluidic channels at the front for multiple chemical deliveries, allowing unobstructed passage for a front light sheet which complements a conventional side light sheet <sup>47</sup> (**Figure 2a, Supplementary Figures 2a, b**). We placed photomasks at both illumination paths to prevent direct exposure to the eyes, thereby avoiding potential distress or tissue damage (**Supplementary Figure 2c**). This microfluidic-dual light sheet configuration enables cellular-resolution imaging of neurons expressing a neuronal activity reporter (e.g., the nuclear-restricted H2B-GCaMP7f calcium indicator) throughout the entire brains of behaving larvae, including the forebrain regions between the eyes (**Supplementary**

**Figure 2d).** Additionally, the setup allows larval subjects, tethered at the head and waist, to freely perform full-range tail flips in a specially designed tail chamber (**Figure 2a**, **Supplementary Figure 2a**).

We performed behavioral and neuronal imaging experiments on larval subjects using the enhanced platform, and obtained stable recordings from five larvae with sufficient repetitions for the delivery of four chemicals (two aversive and two appetitive) (see **Methods**). The experiments consisted of repeated trials of 50-second long imaging, which allowed us to assay spontaneous behaviors from the blank control trials and pre-chemical delivery periods of the stimulus trials (see **Methods** and later **Figure 4a** for details). In the optofluidic system, all five of the larvae displayed robust spontaneous saccades and tail flips, with tail flip frequency comparable to that of freely moving larvae<sup>48</sup> (**Figures 2b, c**). Importantly, our microfluidic-based tethering method yielded more naturalistic behaviors (in terms of saccade and tail flip frequencies) compared to that reported with agarose-based tethering approaches<sup>48,49</sup>. Notably, spontaneous saccades occurred less frequently than spontaneous tail flips, as indicated by the longer median pre-event interval (PEI, defined as difference in onset times between an event and the preceding one) for saccades (5.63 seconds;  $n = 216$  saccades from 5 larvae) vs. tail flips (0.90 seconds;  $n = 1018$  tail flips from 5 larvae) (**Figure 2b**). We integrated the data on saccadic eye movements and tail flip behaviors with concurrent neuronal activity for downstream analysis (**Figures 2d, e**).

### Temporal, directional and kinematic coordination of saccade-coupled tail flips

We first examined spontaneous co-occurrences of saccades and tail flips, defining temporally coupled saccade-tail flip events (hereafter referred to as S-T events) as those with saccade and tail flip onset time difference of 0.5 seconds or less. This threshold is based on it being approximately half the median PEI of the more frequent tail flips. We first examined the relative timings of saccade and tail flip in an S-T event (**Supplementary Figure 3a**). The tail flip typically occurred after the coupled saccade (**Figure 3a**), with their durations largely overlapping (**Figure 3b**), and much shorter latency in offsets compared with onsets (**Figures 3c, d**), indicating that they represent coordinated eye-body movements. Overall, 52.1% of saccades and 15.4% of tail flips occurred in S-T events (**Supplementary Figure 3b**). There is evident temporal coordination in their PEIs compared with when saccades and tail flips occur independently, for which these intervals remained relatively stable (**Figures 3e, f**). Following an S-T event, the PEI for the subsequent saccade increased by about 20%, effectively extending the time for gaze fixation (**Figure 3e**). For tail flips, their PEI around S-T events significantly lengthened, more than doubling in magnitude from 6 prior tail flips to the peak at S-T events, then decreasing back to the baseline over a few tail flips (**Figure 3f**). This pattern indicates that temporal control in S-T events is based on anticipatory and dynamic regulation extending beyond individual occurrence, similar to many other timed behaviors<sup>50</sup>.

During S-T events, saccades and tail flips are predominantly ipsilateral (i.e., towards the same body side) (**Figure 3g**), in line with previous reports<sup>7,8</sup>. Considering the anticipatory nature of S-T events, we investigated the directional synchronization of these movements, by analyzing the directionality of both movements in independent and coordinated events. Consecutive saccades mostly alternated in direction (**Figure 3h**), and

such a pattern did not differ between independent saccades vs. those of S-T events (**Figure 3j**). In contrast, tail flips generally exhibited an ipsilateral tendency relative to each preceding flip (**Figure 3i**) and maintained this pattern across a series of tail flips (**Figure 3k, teal curve**). This aligns with previous findings that the directionality of tail flip is dependent on history<sup>51</sup>. Interestingly, when aligned to S-T events, the dominant direction of tail flip gradually alternated from and to the contralateral side over  $\pm 5\text{--}6$  tails flips (**Figure 3k, coral curve**). As the median pre-saccade interval was also around 6 times that of pre-tail flip interval (**Figure 2b**), this gradual modulation likely permits directional alignment of tail flips with consecutive saccades.

We further analyzed the relationship between S-T events and putative locomotive intent using kinematic parameters of each tail flip extracted from time-series tail angle data (**Supplementary Figure 3c**). The pre-tail flip interval is associated positively with the magnitude and directional bias (**Figure 3l, Supplementary Figures 3d, e**), and negatively with the average undulation interval (**Figure 3m**), of tail flips. Directional bias gradually increased before and peaked at S-T events, followed by a decrease over a few tail flips (**Figures 3n, o**). This pattern appeared to recur approximately every 6–7 tail flips (**Figures 3n, o**). Changes in the average undulation interval exhibited an antiphasic pattern to that of directional bias, peaking at around  $\pm 3^{\text{rd}}$  tails flips relative to S-T events (**Figures 3p, q**). Together, these indicated that S-T events are associated with a greater orientation towards turning (see also similar/related findings in<sup>7,8</sup>) rather than sustained forward gliding<sup>52</sup>, with the kinematics of tail flips modulated in an anticipatory manner along with S-T event timing.

Apart from saccade-coupling, the above-mentioned findings implicated that spontaneous swim bouts are dynamically organized around turns. Using data from our previous study<sup>24</sup>, we first verified the relationship between pre-bout interval and turn magnitude in larvae freely swimming in water (**Supplementary Figure 4a**). We then classified the swim bouts into non-turn and turn bouts (see **Methods**), analogous to the independent and saccade-coupled tail flips, respectively. Upon comparative analysis, we found similar temporal, directional and kinematic coordinations for the turn bouts, but not the non-turn bouts (**Supplementary Figures 4b–e**). The behavioral manifestations of larval zebrafish in a freely moving arena therefore further substantiated that observed in the microfluidic device.

Collectively, we concluded that in larval zebrafish, spontaneous coupled eye-tail flip movements involve highly organized motor coordination. This coordination, occurring through a sequence of tail events, is characterized by simultaneous occurrence of temporal synchronization, directional alignment, and kinematic modulation (**Figure 3r**), putatively for mediating body turns during locomotion.

### Differential impacts of chemical valence on saccade-tail flip coordination

We next aimed to test whether chemical stimuli may influence eye movements and saccade-turn coordination. In response to aversive chemical stimuli, turns may be co-modulated with saccades, and this could in theory manifest in several different yet mutually non-exclusive ways. For example, as S-T events likely mediate turns, the proportion of saccade-coupled tail flips can be increased. In addition, kinematic coordination during S-T

events can be enhanced to make more pronounced turns. On the other hand, turns and forward gliding can also be modulated independent of S-T coordination, by altering the overall directional bias and undulation interval of tail flips. To test these possibilities, we used potent and ethologically representative appetitive or aversive chemical stimuli determined by the previous valence assays, including the death-associated diamines (Cad and Put) and the food-related amino acids (Val and Ala), each at a concentration of 1 mM (**Figure 1c**). Each of these chemicals and a blank control were precisely administered to larval zebrafish for a duration of 10 seconds in a pseudorandomized order with resting intervals during neural-behavioral imaging sessions (**Figure 4a**, see **Methods**).

We first examined the effects of chemical stimuli on saccade, putative turn and forward motion individually. Only the aversive chemicals led to a higher saccade frequency and a lower tail flip frequency during their presentation (**Figures 4b–d**), both of which returned to baseline levels shortly after the cessation of stimulation (**Figures 4c, d**). Consistently, pre-tail flip intervals were the longest during aversive stimuli, and shortest in the presence of appetitive chemicals (**Figure 4e**). During aversive stimuli, the proportion of saccade-coupled tail flips increased (**Figure 4f**), along with an increase in directional bias of tail flips (**Figure 4g**). In contrast, appetitive stimuli did not lead to any discernible change in directional bias (**Figure 4g**). To examine whether larvae may intend to perform more forward swims in response to any chemical stimulus, we analyzed tail flips with  $\geq 4$  undulation cycles. We observed that only appetitive stimuli significantly increased the average undulation duration of these tail flips (**Figure 4h**), presumably leading to more sustained forward gliding movements<sup>52</sup>. Overall, although the individual effects on saccades, tail flips, and stimulus trials appeared modest (**Figures 4b–h**), the cumulative impact of these discrete motor actions could effectively achieve the overarching behavioral goals of pursuit or avoidance.

In the presence of chemical stimuli, the saccades and tail flips during S-T events followed the same temporal and directional alignments (**Supplementary Figure 5**). Tail flips of S-T events during chemical stimuli also exhibited kinematic characteristics distinct from the flanking independent counterparts (**Supplementary Figures 6a–c**). These substantiate a conserved relationship between saccade and body turn. Notably, during aversive chemical-associated S-T events, we observed strong correlations between the magnitude of directional bias and various temporal coupling parameters. Specifically, larger directional biases were associated with shorter latencies between saccade and tail flip onsets and offsets (**Figures 4i, j**), longer durations of overlap between saccades and tail flips (**Figure 4k**), and longer durations of both individual saccades and tail flips (**Figures 4l, m**). Such correlations were absent among S-T events that occurred during blank control or appetitive chemicals (**Figures 4i–m**). These were also not observed when correlating average undulation intervals with the temporal parameters for either appetitive or aversive chemical-associated S-T events (**Supplementary Figures 6d–h**). Furthermore, directional bias, but not average undulation interval, was larger when an aversive chemical-associated S-T event occurred closer to the stimulus onset (**Supplementary Figures 6i, j**). These indicate a heightened coordination between saccades and tail flips specifically in response to aversive stimuli, where tightly synchronized saccade-tail flip events facilitate more intense turning actions.

Taken together, the two opposite chemical valences elicit distinct coordinated behavioral responses in larval zebrafish. Aversive chemicals lead to an increase in saccades and a higher proportion of enhanced, temporally coordinated saccade-coupled tail flips (**Figure 4n**), whereas appetitive chemicals result in more effective forward gliding movements without changes in saccade patterns or tail flip coupling (**Figure 4o**). These highlight the flexibility of the eye-body coordination system in zebrafish larvae, adapting to different chemical cues.

### Brain-wide representation and putative pallial involvement in coordinated eye-body turns

By analyzing the concurrently recorded brain-wide neuronal activities, we aimed to identify neuronal ensembles involved in the control of coupled saccade-tail flips. To this end, we first designed motor regressors for each larva (see **Methods**). By calculating the mutual information (M.I.) between neuronal activity and these regressors, we identified neurons encoding spontaneous tail flips, and determined their preferential involvement in independent vs. saccade-coupled tail flips (see **Methods** for definition of motor preference). This analysis revealed that motor neurons across the brain generally exhibited a preference for independent tail flips, with a notable concentration in key motor command centers, specifically the brainstem mesencephalon and rhombencephalon<sup>53,54</sup> (**Figures 5a, b**). Interestingly, neurons in the telencephalic pallium, a homolog of the cortex in more complex vertebrates<sup>55</sup>, displayed the weakest preference for independent tail flips and the strongest preference for S-T events, compared to other brain regions (**Figures 5a, b**).

We then examined the spatial distributions of chemical valence-encoding neurons (**Supplementary Figure 7**) (see **Methods** for definition of valence preference). Among the primary projection target regions of the olfactory bulbs in the telencephalon<sup>56,57</sup>, we observed distinct activation patterns in response to aversive and appetitive chemicals (**Figures 5c, d, Supplementary Figures 7**). Aversive chemical-elicited activities are channeled through both the pallium and subpallium, whereas appetitive chemicals are well-represented in the subpallium (**Supplementary Figures 7a–d**). This subpallial appetitive preference mirrors the reported stronger response to mating water compared with skin extract in the juvenile zebrafish subpallium<sup>27</sup>. In most downstream regions, positive valence was represented by larger numbers of neurons (**Figures 5c, d, Supplementary Figures 7a–d**). In parallel to its preference for spontaneous S-T events in motor control, the pallium also exhibited a more pronounced representation of negative valence compared with other brain regions (**Figures 5c, d**). Of note, although neurons involved in spontaneous S-T event and negative valence representation were outnumbered, they exhibited significantly higher activation levels compared with the counterparts encoding independent tail flips and positive valence, respectively (**Figures 5e, f**).

Next, we analyzed the neuronal sensorimotor preferences to understand how individual neurons encode both motor actions and chemical valence (**Figures 5g–j, Supplementary Figure 8a**). For each neuron, we calculated a joint preference measure as the  $L^2$  norm of a two-dimensional vector consisting of the two preference measures (i.e., [motor preference, valence preference], used in **Figures 5a, c**) (see **Methods** for details). We used

the measure to quantify a neuron's preferential responsiveness to either S-T events combined with aversive stimuli, or independent tail flips combined with appetitive stimuli. This analysis further illustrated that the pallium exhibited the strongest overall preferential co-encoding of spontaneous S-T events and negative valence (**Figures 5g, h, Supplementary Figures 8b, c**). In contrast, more caudal brain regions better co-represent spontaneous independent tail flips and positive valence (**Figures 5i, j**).

We further examined the temporal dynamics of pallial activity in relation to chemical cue-associated S-T events. Specifically during aversive cues, pallial motor-encoding neurons exhibited early activation preceding tail flip onset in S-T events, but not during appetitive chemicals presentation (**Figure 5k, upper, Supplementary Figure 9**). This was also noted in rhombomeres 4 and 6 (**Supplementary Figure 9**), but not in the other brain regions (**Figure 5k, upper, Supplementary Figure 9**).

In the telencephalon, pallial motor activations were more prominent for aversive chemical-associated S-T events with a higher temporal proximity of saccade and tail flip onsets (**Figure 5k, lower, Supplementary Figure 10a**), or aversive chemical stimulus and tail flip onsets (**Supplementary Figure 10b**). This neural activity pattern aligns with the behavioral observations that tail flip directional bias inversely correlated with saccade-tail flip onset delay (**Figure 4i**), as well as aversive chemical-associated S-T event onset delay from stimulus onset (**Supplementary Figure 6i**). Interestingly, these were not observed for rhombomeres 4 or 6, where the early motor activations appeared independent of these event proximities (**Supplementary Figures 10a, b**). These observations indicate a sensorimotor role for pallial motor-encoding neurons, potentially mediating the increase in tail flip directional bias and strengthening of saccade-tail flip coupling by aversive cues. In contrast, the activation patterns in rhombomeres 4 and 6 suggest a premotor role for subsets of neurons in these hindbrain regions, possibly driving S-T events independently of their temporal proximity to the initiation of aversive chemical stimulus.

In contrast to S-T events, independent tail flips exhibited distinct associated neuronal activity patterns. These were characterized by a lack of early pallial activation relative to tail flip onset during aversive cues presentation (**Figure 5l, Supplementary Figure 11**). Instead, independent tail flips were associated with early neuronal activations in the preoptic area, pretectum, tectum, rhombomere 7, and caudal hindbrain, particularly during appetitive stimuli (**Supplementary Figure 11**). This differential activation pattern further underscores the unique role of pallium in coordinating S-T events, especially in response to aversive stimuli.

Collectively, these findings align with and provide a neural basis for the aversive chemical-specific enhancement of saccade-tail flip coordination observed behaviorally (**Figures 4i–m, Supplementary Figure 6i**). They also highlight the larval zebrafish pallium as a key sensorimotor hub in integrating sensory information and motor outputs.

## Discussion

Chemosensation, one of the most ancient and conserved sensory mechanisms, has guided body movement and locomotion from the earliest life forms on Earth to the complex

organisms of the Ediacaran and Cambrian periods<sup>58</sup>. It predates both vision and the development of movable body parts such as simple lens eyes and appendages (e.g., tails or limbs) in animals<sup>59</sup>. While the influence of sensory cues other than vision and mechanosensation on eye-body coordination had not been well-understood, we provide behavioral evidence and neuronal correlates demonstrating its modulation by chemosensory cues in developing larval zebrafish. These highlight the integrated roles of chemosensation and vision in animal locomotion, a synergy that likely emerged over 450 million years ago<sup>60</sup>.

Larval zebrafish swim and make body turns in discrete bouts. This pattern of discrete movements, common in many developing animal species, plays a foundational role for locomotive behaviors during development<sup>61</sup>. The control of the more frequently occurring tail flips lays the groundwork for eye-body coordination, which requires precise temporal modulation and mechanical tuning. While saccades typically align with peak body turns, forward gliding primarily occurs during periods of gaze fixation, accompanied by continuous timing and kinematic adjustments across consecutive tail flips. The anticipatory nature, along with the fine time scale of body turn magnitude, indicate a highly sophisticated control mechanism underlying locomotion and navigation.

Our findings also reveal that in larval zebrafish, eye-body coordination is highly adaptable to external stimuli. In tail flips, these adaptations manifest as kinematic changes tied to temporal coupling with saccades, aligning with collective behavioral strategies for avoidance or pursuit based on perceived chemical cues. Specifically, the detection of negative chemical valences triggers enhanced saccades and more pronounced body turns, whereas positive valences are associated with more efficient gliding movements during independent tail flips. In response to chemosensory inputs, larval zebrafish thus demonstrate a more active selection of motor programs consisting of coordinated eye-body movements. This should allow them to optimize their locomotion, ensuring appropriate responses to chemical cues of varying valence.

Regarding neuronal correlates, our findings revealed that negative chemical valence is strongly represented in dedicated olfactory and downstream relay circuits that likely enhances the initiation of chemosensory-driven, saccade-coupled turns. We showed that the process is associated with sensorimotor activity in the higher-order cortical homolog pallium<sup>55</sup>. The integration of chemosensory processing with motor program execution underscores its critical role in orchestrating adaptive behaviors in larval zebrafish. Recent studies have highlighted the pallium's multifaceted functions, including sleep regulation<sup>62</sup>, place encoding<sup>63</sup> and spatial representations<sup>64</sup>. Altogether, these findings suggest that even at this early developmental stage, zebrafish possess a remarkable ability to process environmental information and translate it into precisely coordinated motor outputs, with the pallium playing important roles.

This work opens avenues for further studies on sensory input-mediated eye-body control. While coordinated eye and body movements are common across many species, their patterns exhibit significant variations depending on species<sup>5</sup>, developmental stages, and environmental conditions. Unlike teleosts, which lack necks<sup>40,41</sup>, other vertebrates likely rely more on head and neck movements for sensorimotor coordination. Future research should

extend these investigations to diverse species, and explore both a wider range of chemosensory stimuli and additional sensory modalities<sup>65</sup>.

## Methods

### Animals

All experimental procedures received prior approval from the Animal Research Ethical Committee of the Chinese University of Hong Kong (CUHK) and complied with the Guide for the Care and Use of Laboratory Animals. For this study, *nacre*-mutant larvae, aged 5–8 days post-fertilization (d.p.f.), were raised and maintained under a 14-hour light/10-hour dark cycle at a constant temperature of 28°C. Larvae used for experiments were not fed, as per common practice and this does not compromise their health at this developmental stage<sup>66</sup>. The larvae used in the valence determination assay ( $n = 313$ ) were bred from adult zebrafish pairs with at least one heterozygous Tg(elavl3:GCaMP6f) parent and were not screened for GCaMP6f expression. The larvae used in the behavioral and neuronal imaging assays ( $n = 5$ ) were bred from Tg(elavl3:H2B-GCaMP7f) adults and were screened for the presence of GCaMP7f expression. The sex of larvae was not determined at this stage of development.

### Fluidics-based swimming arena for chemical valence determination

The device was designed using AutoCAD 2020 (Autodesk, USA) and comprised five 1.5 mm-thick layers of laser-engraved poly(methyl methacrylate) (PMMA). The layers were meticulously aligned vertically and fused by applying a chloroform solution along the contact edges, which yielded a durable, sealed structure. This process formed a closed square arena with dimensions of 40 mm in length and 1.5 mm in height (Figure 1a). An additional inlet was used for loading larvae and sealed prior to assays. The inlets and outlets are 200 µm wide, prohibiting larvae from exiting the arena through these channels. Fluidic connections were established by securing syringe needles (Terumo, USA) to the topmost PMMA layer with an epoxy adhesive paste (Devcon, USA). These needles were linked to the inlet and outlet channels, which in turn connected to syringes containing the fluid stimuli and to a waste collection bottle, respectively. The connections were facilitated using poly(tetrafluoroethylene) (PTFE) tubing (Cole-Parmer, USA). After construction, the device was left to air-dry for 24 hours, allowing for the complete evaporation of residual chloroform and epoxy adhesive paste. To ensure the device was contaminant-free, it was washed thoroughly with water twice, thus removing any potential contaminants prior to its use in behavioral assays.

Defined chemical zones within the arena were created using four fluid streams, each channeled through inlet channels located at the corners of the arena and propelled at a constant flow rate of 100 µL/min by precision syringe pumps (LSP02-2A, Longerpump, Beijing). The background solvent of these fluid streams was either water or a 0.5% DMSO solution, depending on the tested chemical species. Chemicals with limited water solubility, including prostaglandin F2α (PGF2α), chenodeoxycholic acid (CDCA), and glycodeoxycholic acid (GDCA), were dissolved in 0.5% DMSO solution to ensure complete dissolution. This concentration of DMSO has been determined to be safe for the larvae and does not affect their baseline behaviors<sup>67</sup>. Other chemicals were dissolved in water.

The top right control quadrant (quadrant I) contains no chemicals, while the remaining quadrants contain chemical species at varied concentrations (**Figures 1a, b**). For the three chemical species with limited solubility, both water and 0.5% DMSO were used as controls in separate assays (**Supplementary Figures 1b, c**). The outlet of the arena was connected to an open waste collection bottle to allow for the efficient disposal of the outflow fluids.

The Reynolds number ( $Re$ ) of fluid flow in the arena is given by  $Re = \rho v D_H / \mu$ , where  $\rho$  is the fluid density,  $v$  is the fluid flow velocity,  $D_H$  is the hydraulic diameter of the device, and  $\mu$  is the fluid dynamic viscosity. Given the average cross-sectional dimensions at each quadrant of the arena (i.e.,  $1.5\text{ mm} \times 10\sqrt{2}\text{ mm}$ ), the corresponding average flow rate was  $100\text{ }\mu\text{L min}^{-1}$  or  $1.67\text{ mm}^3\text{ s}^{-1}$ . Hence the average flow velocity =  $1.67\text{ mm}^3\text{ s}^{-1}/(1.5\text{ mm} \times 10\sqrt{2}\text{ mm}) = 7.86 \times 10^{-5}\text{ m s}^{-1}$ .  $D_H$  for the rectangular channel is given by  $2ab/(a+b) = 2.71 \times 10^{-3}\text{ m}$ , where  $a$  and  $b$  are the average dimensions of the rectangular cross-sections (i.e.,  $1.5\text{ mm}$  and  $10\sqrt{2}\text{ mm}$ ). Substituting the  $D_H$  found, and the density ( $996\text{ kg m}^{-3}$ ) and the dynamic viscosity ( $8.32 \times 10^{-4}\text{ Pa.s}$ ) of water at  $28\text{ }^\circ\text{C}$ , the Reynolds number was found to be  $Re = 0.255 \ll 2000$ . As  $Re \ll 2000$ , the streams were laminar with negligible mixing<sup>68</sup> and static fluid zone borders were formed. The Péclet number ( $Pe$ ) of fluid flow in the arena is given by  $Pe = vD_H/D$ , where  $D$  is the diffusion coefficient of the molecule. Since all the investigated small molecules have diffusion coefficients of the  $10^{-9}\text{ m}^2\text{s}^{-1}$  range order,  $Pe \approx 2.13 \times 10^2 \gg 1$ , the molecules thus have minimal diffusivity across the streams. The  $Re$  and  $Pe$  values suggest that the chemicals delivered using the system would be minimally crossing via advection and diffusion, respectively, and therefore stay highly localized within individual fluid streams. As the geometry and flow profile of the four quadrants are identical, four identical static chemical zones are established. The chemical zones were visualized by infusing an IR dye (IR 806, Sigma, USA) into the quadrant II and IV of the device (**Figure 1a, lower**).

#### *Chemical valence determination assay*

During a chemosensory valence determination assay, three to six zebrafish larvae aged 5–8 days post fertilization (d.p.f.) were placed in a swimming arena and allowed to acclimate for 15 minutes before the introduction of chemical stimuli. To minimize potential visual cues across different assays, the arena was horizontally rotated to a single angle of  $0^\circ$ ,  $90^\circ$ ,  $180^\circ$ , or  $270^\circ$  in a pseudo-randomized manner for each assay. To further reduce these cues, the recording was conducted under 850-nm IR illumination (ANGX-1000-CH1-24V, TMS, Maalysis) in the absence of visible light. Time-lapse video was recorded by a CCD camera (Mako G-040B PoE, Allied Vision, Germany) at 20 frames per second, with image acquisition managed by Stremppix 7 (Norpix, Canada). The recording lasted for 30 minutes, with four fluid streams flowing at the same speed. The fluid temperature was maintained at  $\sim 28^\circ\text{C}$  throughout the assay. This assay enables precise behavioral monitoring of the larvae, ensuring that the specific chemical exposure was exactly known, thereby minimizing potential biases in hedonic measurements.

## *Microfluidic device for multichannel precise chemical simulation, saccade, tail flip and brain-wide cellular-resolution imaging*

Capturing the behaviors and neural activity elicited by chemosensory cues presents a significant challenge in the field. In our previous development of Fish-On-Chips<sup>24</sup>, we enhanced the precision of a single chemical cue delivery to larval zebrafish, enabling stable recordings of neuronal responses to chemosensory inputs. In this work, we further developed the platform with the objective of systematically exploring the impact of multiple ecologically pertinent, valence-inducing chemicals on the natural behaviors of larval zebrafish and uncovering the associated neural circuitry.

Compared with our previous device, we further optimized the channel design in order to achieve multiple chemical delivery, compatibility with dual-scanning light sheet imaging and maximize the behavioral readout to include both saccade and tail flip. The PDMS-based microfluidic device was designed in AutoCAD 2020 (Autodesk, USA). It was then fabricated by customized photolithography techniques like the previous ones to incorporate flat transparent sidewalls at the front and the right side with respect to the head chamber to accommodate for the entry of two scanning excitation light sheets, and a thin glass ceiling for the emitted fluorescence detection path. Briefly, a 2D design was printed on a soda lime mask (Supermask, Shenzhen). Negative photoresist SU-8 2150 (Microchem, USA) was spin-coated on a 4-inch silicon wafer (Semiconductor Wafer, Taiwan) to 500- $\mu\text{m}$  thick. The device pattern was then transferred to the photoresist with UV exposure (OAI, USA), followed by post-exposure bake and etching to produce a master mold. Mixed PDMS (Dow Corning, USA) and curing agent (at 10:1 w/w) were poured into the salinized mold to a thickness of 5 mm, with perpendicular glass slides held upright on the mold to produce the front and the right side flat vertical surfaces upon curing. After solidification at either 65°C for 240 minutes or 100 °C for 60 minutes, it was detached from the mold, bonded and sealed onto a microscopic cover slide (as thin glass ceiling) by plasma treatment. All devices were rinsed with water twice before use in experiments.

The fluidic stream control solution was similar to our previous design. In brief, bilaterally three-layered, sandwiched fluid streams are directed to the larval zebrafish from the sides and converge at the middle, and then leave the device. The middle stream was switched to different solutions to allow selections of chemicals in different trials. Each fluid stream was carried by PTFE tubes, controlled by a solenoid valve (LHDA 0533115H, Lee Company, USA), and driven by a syringe pump. A side channel connecting the chemical delivery microchannels and the tail chamber was incorporated to buffer pressure changes in the fluidic environment, and minimize mechanical disturbances to the larval subject. The flow rate was uniformly adjusted at 80  $\mu\text{L}/\text{min}$ , which yields the same order magnitude of  $Re$  and  $Pe$  numbers, and thus allows for highly controlled fluid delivery. The details of the valve control and chemical delivery are described in the following sections.

Through iterative experimentation, we determined the necessity for bilaterally independent channels to achieve symmetrical stimulus rise and fall times. One challenge we noted was the natural formation of micro-sized air bubbles during fluid coalescence, which can interfere with the accuracy of fluid delivery. The likelihood of bubble formation scales

with the number of fluid inlets. We optimized the design to include a total of 7 channels on each side, using the first and last channels for water streams (sandwiching the chemical streams), and 5 channels dedicated to different chemical streams (**Figure 2a**).

These significant enhancements, together with other minor ones, enabled us to systematically deliver 4 different water-soluble chemicals plus 1 blank water control for 4–6 repeated trials each. We ensured a 10-second exposure duration for each stimulus trial to allow sufficient time for the larval subjects to exhibit saccadic and tail flipping responses, which differed greatly in event frequency. Additionally, we also ensured a 10-second imaging time after each stimulus was removed. This setup was optimal for multi-trial simultaneous behavioral-neuroimaging experiments, allowing for approximately one hour total assay time per larval subject. We anticipate incorporating additional channels and an even more streamlined experiment paradigm with further developments.

#### *Dual-scanning light sheet fluorescence microscope for whole-brain calcium imaging*

We custom-built a light sheet fluorescence microscope with two light sheet excitation paths from the front and right side of the larval subject for optimized cellular-resolution whole-brain imaging. For each of the excitation paths, a 486 nm-centered blue gaussian laser (DL-488-050-0, Crystalaser, USA) was used as the excitation light source. The laser beam was resized to 0.6 mm in diameter ( $1/e^2$ ) by a pair of telescopic lenses (LB1757-A, LB1596-A, Thorlabs, USA), which then passed through a scanning system, followed by a cylindrical lens (LJ1695RM-A, Thorlabs, USA) that focused the horizontal dimension of the parallel beam onto the back focal plane of an air excitation objective (Nikon Plan Fluorite,  $\times 10$ , N.A. 0.3, 16 mm WD). This expanded the laser horizontally to form a light sheet. The scanning system consisting of a galvanometric mirror (GVS211/M, Thorlabs, USA), a F-theta lens (S4LFT0061/065, Sill Optics, Germany) and a tube lens (TTL200-A and TTL200-B, Thorlabs, USA) was used to scan the light sheet vertically and linearly over a range of 276  $\mu\text{m}$ . The F-theta and tube lenses also expanded the beam 3.31 times, resulting in a beam diameter of 2 mm ( $1/9^{\text{th}}$  of the objective back aperture) and effective excitation N.A. of 0.0332. A photomask with a 250  $\mu\text{m}$  aperture and a photomask with an open-ended aperture (**Supplementary Figure 2c**) were placed and aligned at the front and at the right side of the device respectively to avoid directly shining the eyes of the larval subject with either light sheet at either side.

Along the detection path, a bandpass green filter ( $525 \pm 25 \text{ nm}$ ) was placed after an air detection objective (TL10X-2P, Thorlabs, USA;  $\times 10$ , N.A. 0.5, 7.77 mm WD) to block the blue excitation light. An electrically tunable lens (EL-16-40-TC-VIS-20D-1-C, Optotune, Switzerland) was linearly driven by a lens controller (TR-CL-180, Gardasoft, UK) and synchronized with the light sheet scanner to achieve rapid focusing of different image planes onto the sensor of a sCMOS camera (Panda 4.2, PCO, Germany). During an experiment, to correct for axial drift, a reference plane was calibrated with respect to the initial measurement at the beginning of each trial. All control units were synchronized using a multifunctional I/O device (PCIe-6323, National Instruments, USA) and custom-written codes in MATLAB (R2018b, MathWorks, USA).

#### *Simultaneous whole-brain calcium imaging and behavioral recording*

To obtain the most naturalistic data, we only included larvae that were nearly perfectly leveled in the device (evidenced by the two eyes at the same level) for further experimentation and analysis. A total of five larvae aged 5–6 days post fertilization (d.p.f.) from three batches of breedings were included. Each of the five robustly behaving zebrafish larvae underwent simultaneous behavioral and whole-brain neuronal calcium imaging experiments in an upright orientation as permitted by the improved imaging set-up.

In an imaging experiment, a larva was loaded (via the larva inlet) and fitted into the trapping chamber of the PDMS-based microfluidic device using a syringe pump and monitored under a surgical microscope. Then, the larva was allowed to acclimate for 15 minutes. Introduction of bubbles to the microfluidic system was carefully minimized during system setup to avoid unwanted fluid flow pattern changes or mechanical instability of the larval subject. Prior to functional imaging, a detailed anatomical stack of the larval zebrafish brain spanning 138 imaging planes at 2- $\mu$ m intervals was taken. In this intact upright imaging configuration, the majority of the brain except the topmost (e.g., habenula) and bottommost regions (e.g., caudal hypothalamus) which are directly under the cover glass slide and furthest from the detection objective lens, was consistently imaged across larvae.

During functional imaging, whole-body saccadic and tail flipping behaviors (single-plane, at 200 Hz) and volumetric whole-brain calcium fluorescence signals (28 planes with 7- $\mu$ m intervals, at 2 Hz) were simultaneously imaged under chemosensory cue (or blank control) delivery. Behavioral images were acquired under IR illumination by a CCD camera (Mako G-040B PoE, Pike, Germany) and the Stremppix 7 (Norpix, Canada) image acquisition software, while calcium images were acquired with the abovementioned custom dual-light sheet scanning microscope. Each larva underwent 23–30 experimental trials with a total of five types of stimuli. These stimuli include amino acids (valine and alanine), diamines (cadaverine and putrescine), all at one millimolar concentration, and a blank control. Each stimulus was delivered bilaterally to both nostrils for 4–6 repetitions. Each trial lasted for 50 seconds with 30-second baseline, 10-second stimulus presentation, and 10-second post-stimulus recording periods, followed by ~90-second inter-trial resting intervals. Axial drift corrections were then performed in between trials.

During each 30-second baseline recording period, in the three-layer sandwiched fluid streams, the middle stimulus stream carried a chemical cue (or water for blank control trials). The first (water) and the second (stimulus) stream in front of the nostrils were then switched off sequentially by the respective controlling valves at the two sides, with 10-second gap to allow the second (stimulus) and the third stream (water) to contact the nostrils. This resulted in the initiation and termination of chemical stimulation. Recording continued for 10 seconds after stimulus cessation.

#### *Valence determination analysis (swimming arena)*

Individual frames of the navigation behavioral tracking videos were first registered for translation, background-subtracted, and contrast-adjusted. The *xy*-coordinates of the heads of larvae in each frame were extracted using our previously established semi-automated template matching-based tracking program <sup>24</sup> custom-written in MATLAB (R2018b, MathWorks, US). All tracking results were manually verified on a frame-by-frame basis and

corrected when necessary. The coordinates were then used to calculate the proportions of time spent in each of the same-area quadrants over the 30-minute recording time. Additionally, since there is minimal mixing across streams under laminar flows, interactions between quadrants containing the same chemical at different concentrations were negligible. The population standard deviation of the time spent difference in chemical quadrants (compared with the control quadrant) of the setup was estimated from the sample standard deviation of the time spent difference in the control group with Bessel's correction.

#### *Behavioral image processing and analysis (microfluidic device)*

Eye and tail movements were extracted from behavioral images by a custom MATLAB program (R2018b, MathWorks). The first ten seconds of the behavioral recordings of each trial were excluded from analysis to avoid confounding behaviors evoked by the onset of light sheet illumination. In addition, a total of six trials, three trials each from two subjects, were found to have bubbles present, which disrupted the laminar flows necessary for precise chemical delivery. These trials were also discarded. For eye movements, the video was down-sampled by a factor of 25 times (resultant frame rate: 8 fps) to achieve a higher signal-to-noise ratio. The turn direction and duration of the saccades were manually identified using rotational visual flows in each region-of-interest of the two eyes. Only two events (out of 595 events recorded from 5 larvae) of bilateral eye movements from one larva were recorded with incoherent eye movement directions, and these were excluded from analysis. Pre-saccade interval was defined as the time between the onset of a saccade and that of its preceding one, if both were recorded.

For tail movements, episodes of tail flips were identified based on changes in tail tip-waist angle using several criteria. An episode was isolated when tip-waist angle changes occurred in at least two consecutive frames (frame rate: 200 fps), and were temporally situated before and after at least three frames of stationary angle changes. The start and end frames were determined as the last frame of the last idle period and the first frame of the next idle period, respectively. Positive and negative peaks in the undulating cycles of angle changes were identified using the built-in *findpeaks* function in MATLAB (R2018b, MathWorks, USA). The undulation cycle was determined by averaging the number of positive and negative peaks.

Pre-tail flip interval was defined as the time between the onset of a tail flip and that of its preceding one, if both were recorded. Tail flip duration was calculated as the time difference between the end and start frame of an episode. The average undulation interval was calculated by dividing the duration by the undulation cycle. Magnitude and directional bias were calculated using the sum and difference of the average net positive and average net negative peaks, respectively, with the zero reference being the average of the start and end angles (**Supplementary Figure 3c**). A small non-zero average directional bias to the right side was consistently observed in the spontaneous tail flips of the five subjects ( $2.6^\circ \pm 1.2^\circ$  (mean  $\pm$  S.D.)), which was due to the asymmetrical illumination from the right side. Directional bias calculation was adjusted by subtracting each subject's average directional bias.

Tail flips were classified based on directional bias. A tail flip with a bias of  $\geq 1.5^\circ$  (one-half of the median bias of all spontaneous tail flips) was considered a turn event. If the bias was  $< 1.5^\circ$ , it was classified as a non-turn event. In the laterality analysis of tail flips (**Figures 3g, i, k, Supplementary Figures 5e, g, l, n, s, u**), only turn events were included for comparisons. Non-turn events, indicating forward movement, were excluded from this analysis.

A tail flip was defined as saccade-coupled (S-T events) if the onset occurred within 0.5 seconds of a saccade's onset (i.e.,  $|T\text{-ON} - S\text{-ON}| \leq 0.5$  seconds). For each saccade, only the tail flip with the closest onset was considered saccade-coupled. S-T events with saccade onset certainly later than the tail flip onset, defined as those with  $T\text{-ON} - S\text{-ON} < -0.0625$  seconds with the temporal error of saccade time determination considered, represented a small subset (11 out of 172) of all spontaneous S-T events (**Figure 3a**). This pattern was largely conserved for chemical-associated S-T events (appetitive: 4 out of 33, aversive: 3 out of 32, **Supplementary Figures 5h, o**). These were not included for the regression analysis of S-T coordination (**Figures 4i–m, Supplementary Figures 6d–j**).

Events recorded during blank trials were classified as spontaneous. During chemical stimulation trials, events were considered spontaneous if the onset was recorded before the stimulus onset, and the offset was recorded before or coincided with the stimulus onset. Events were considered to be stimulus-evoked if the onset occurred later than stimulus onset, and the offset occurred before or coincided with the stimulus offset. Onset and offset of S-T events were defined as that of the saccade. Events during the resting intervals between trials were not recorded or analyzed.

Pre-event interval was defined as the time difference between the onset of a saccade, a tail flip, or a bout and that of the respective preceding one (**Figures 2b, c, 3e, f, l, m, 4e, Supplementary Figures 3d, 4a, 6c**). For comparison with flanking events (**Figures 3e, f, j, k, n–q, Supplementary Figures 4b, d, e**), saccades and tail flips were first categorized into either S-T or independent groups and set as the 0<sup>th</sup> next event. For each 0<sup>th</sup> next event, the sequence and quantity of other events (n<sup>th</sup> next event) were shown. An event could be the 1<sup>st</sup> next event for one sequence and the 2<sup>nd</sup> next event for another, causing overlaps.

#### *Comparative analysis based on previously acquired data of freely swimming larvae*

A dataset from our previous study was used <sup>24</sup>. In that study, 11 larvae in 3 assays were allowed to swim in the absence of visible light for 2 hours in a 2D rectangular arena (60 mm  $\times$  30 mm  $\times$  1.5 mm) completely filled with still water, and imaged under IR illumination. The heading orientation (10° resolution) of every larva in each frame was extracted using a semi-automated template matching-based tracking program custom-written in MATLAB (R2018b, MathWorks, US). All bouts subsequent to the first bout in the rightmost virtual chemical zone of the arena were extracted for analysis. Pre-bout interval was defined as the time difference between the onset of a swim bout and that of its preceding bout. Turn angle was defined as the orientation change in either direction. A swim bout was defined as a turn bout based on the turn angle  $\geq 70^\circ$ , and non-turn bout otherwise. Only swim bouts with an orientation change were used to compare the proportion of consecutive ipsilateral turns (**Supplementary Figures 4c, d**).

### *Calcium image processing and signal extraction*

We adopted an analysis pipeline similar to our previous work<sup>24</sup>. Detailed larval zebrafish brain anatomical stacks were registered to the Z-Brain Atlas<sup>69</sup> using affine transformation followed by non-rigid image registration using custom scripts written in MATLAB (R2018b, MathWorks, USA). Functional imaging planes were matched to the corresponding anatomical stack by maximization of pixel intensity cross-correlation and manually verified. Stripe artifacts in the anatomical stacks and functional imaging frames were removed using the Variational Stationary Noise Remover (VSNR) algorithm<sup>70</sup>. Functional imaging frames were motion-corrected using discrete Fourier transform and NoRMCorrE algorithms<sup>71</sup>. Trials with blurred frames due to in-frame drifts were discarded. Region of interest (ROIs) corresponding to individual neurons were then extracted using the CaImAn package<sup>72</sup>. Anatomical landmarks and the regional identity of each ROI were verified by manual inspection (by S.K.H.S.). Note that this only included neurons that had fired at least once during all imaging sessions and with a sufficiently high signal-to-noise ratio determined by the CaImAn-based analysis pipeline.

Trials with unsatisfactory image registration were excluded from further analysis. For one larva with more jitters in the functional images, the images stack were initially downsampled to 1 Hz by averaging every two consecutive frames. For trials with plane-specific jitters, a small proportion of frames with jitters were replaced with the immediate preceding frame (or the next frame if the preceding frame also had jitter) for the data from all larvae. Trials with more than two consecutive jittering frames were excluded from further analysis. In total, we retained whole-brain neuronal imaging data from 88 out of 139 trials from the five larvae that passed all quality control criteria.

### *Identification of motor- and sensory-coding neurons*

The first 10.5 or 11 seconds (21 or 11 imaging frames) of the imaging data of each trial were excluded from analysis to avoid the inclusion of transient activity evoked by the onset of light sheet illumination. The minimum fluorescence intensity in the subsequent 4.5 or 4 seconds (9 or 4 imaging frames) of each ROI was used as the baseline fluorescence (F). The  $\Delta F/F$  signals of the remaining imaging frames were calculated as the calcium response of each ROI.

Motor and sensory regressors were designed to identify motor- and sensory-encoding ROIs. Motor output was defined to be the proportion of frames with active tail flip in each 0.5-s or 1-s imaging time bin, and a motor output regressor was created to represent this (motor regressor 1). A second motor regressor for independent tail flips was created by excluding all tail flips of S-T events (motor regressor 2). A third regressor was designed by randomly removing tail flip events from motor regressor 1 at a probability that corresponded to each larva's S-T event proportion (motor regressor 3). Utilizing these three regressors allowed us to directly identify both the saccade-coupled and independent tail flip-encoding neurons but avoided saccade-encoding neurons<sup>7,49</sup>. Chemical stimulus regressors were created with a step function during the stimulus window of each chemical. All regressors are normalized to the [0, 1] range. We calculated the mutual information ( $I$ ) between the calcium responses of each ROI and the regressors by a method based on kernel density estimation of

the probability density functions of variables<sup>73</sup>. For motor mutual information, only all the imaging frames in the entire blank trials and before stimulus onsets in stimulus trials were used for calculation. For sensory mutual information, all imaging frames were used. With the three motor (**Table 1**) and five chemical stimulus regressors, each ROI had eight mutual information values, namely  $I_{\text{tail\_flip\_all}}$  (based on motor regressor 1),  $I_{\text{tail\_flip\_independent}}$  (based on motor regressor 2),  $I_{\text{tail\_flip\_randomRemove}}$  (based on motor regressor 3), as well as  $I_{\text{valine}}$ ,  $I_{\text{alanine}}$ ,  $I_{\text{cadaverine}}$ ,  $I_{\text{putrescine}}$ , and  $I_{\text{blank}}$  (for which the suffix denotes the chemical or blank control). These values were used to determine significant motor and/or sensory information encoding, and calculate the motor and valence preferences (see the next sections).

**Table 1.** List of motor regressors and mutual information measures.

<i>Regressors</i>	Motor regressor 1, includes all tail flips	Motor regressor 2, excludes S-T events, i.e., all independent tail flips only	Motor regressor 3, excludes random tail flip events matching S-T proportion
<i>Mutual information</i>	$I_{\text{tail\_flip\_all}}$	$I_{\text{tail\_flip\_independent}}$	$I_{\text{tail\_flip\_randomRemove}}$

To estimate the distributions of the mutual information values expected under randomness, we shuffled the  $\Delta F/F$  signals of each ROI (i.e., disrupting their temporal structures) and calculated another set of shuffled values. We defined the motor- and sensory-encoding neurons to be those that most significantly encode behavior variables or chemical stimuli. Motor-encoding neurons were defined as ROIs with either  $I_{\text{tail\_flip\_all}}$  or  $I_{\text{tail\_flip\_independent}} > 1.3$  times 99<sup>th</sup> percentile of the shuffled  $I_{\text{tail\_flip\_all}}$  or  $I_{\text{tail\_flip\_independent}}$ , respectively. Sensory-encoding neurons were defined as those with at least one  $I_{\text{chemical}} > 1.3$  times the 99<sup>th</sup> percentile of the shuffled  $I_{\text{chemical}}$  (where the suffix refers to one of the four chemicals). ROIs with  $I_{\text{blank}} > 1.3$  times the 99<sup>th</sup> percentile of the shuffled  $I_{\text{blank}}$ , representing neurons that putatively responded to valve and/or fluid velocity changes, were excluded. ROIs with both significant  $I_{\text{valine}}$  and  $I_{\text{alanine}}$  were defined as appetitive chemical-encoding neurons, and ROIs with both significant  $I_{\text{cadaverine}}$  and  $I_{\text{putrescine}}$  were defined as aversive chemical-encoding neurons. Valence-encoding neurons were defined as the union of appetitive and aversive chemical-encoding neurons.

#### *Calculation of motor and valence preference for each neuron*

Each of the mutual information values were normalized by dividing by the 99<sup>th</sup> percentile of the corresponding shuffled values (for simplicity of notation, hereafter referred to using the original symbols). Motor preference was defined for each motor-encoding neuron by the equation:

$$\text{Motor preference} = I_{\text{tail\_flip\_randomRemove}} - I_{\text{tail\_flip\_independent}}. \quad (1)$$

A higher value ( $> 0$ ) of this quantity indicates stronger S-T event encoding, as mutual information kept after random tail flip removal (note the above-mentioned matching to S-T event proportion) is more than that with complete S-T removal. Conversely, a lower value ( $< 0$ ) of such indicates stronger independent tail flip encoding, as more mutual information is kept with complete independent tail flip preservation than random removal that reduced

independent tail flips while keeping some S-T events. Valence preference was defined for each sensory-encoding neuron by:

$$\begin{aligned} \text{Valence preference} &= \frac{I_{\text{cadaverine}} + I_{\text{putrescine}}}{2} - \frac{I_{\text{valine}} + I_{\text{alanine}}}{2} \\ &= I_{\text{aversive}} - I_{\text{appetitive}}. \end{aligned} \quad (2)$$

The norm of sensorimotor preferences was calculated for each unit of the union set of motor- and valence-encoding neurons that were S-T- and aversive valence-preferring (i.e.,  $I_{\text{tail\_flip\_randomRemove}} - I_{\text{tail\_flip\_independent}} > 0$  and  $I_{\text{aversive}} - I_{\text{appetitive}} > 0$ ), or independent tail flip- and appetitive valance-preferring (i.e.,  $I_{\text{tail\_flip\_randomRemove}} - I_{\text{tail\_flip\_independent}} < 0$  and  $I_{\text{aversive}} - I_{\text{appetitive}} < 0$ ) by the equation:

$$\text{Norm of sensorimotor preference} = \sqrt{\text{Motor preference}^2 + \text{Valence preference}^2}. \quad (3)$$

### *Data visualization*

All smoothing was performed using the built-in *smooth* function in MATLAB (R2018b, MathWorks, USA), with span of moving average = 3 (**Figures 3f, k, n-q, 4d, Supplementary Figures 4b, d, e**). In the time-series stimulus-evoked plots (**Figures 4c, d, f**), time bins were chosen as 5, 0.83, and 2 seconds, according to the event rates of saccade (**Figure 4c**), tail flip (**Figure 4d**) and S-T events (**Figure 4f**), respectively. Each bin includes the trailing but not the leading edge. Quantities were normalized by subtracting the average binned values in the 10-second pre-stimulus windows. Tail flip frequency was normalized to and expressed as the number of standard deviations of the binned pre-stimulus frequency (**Figure 4d**).

For the mean response of motor-encoding and valence-encoding ROI (**Figures 5e, f**), each range includes the trailing but not the leading delimiter. For the motor response trace shown (**Figures 5e, k, l, Supplementary Figures 9–11**), the linear trend of  $\Delta F/F$  before the tail flip event ( $t = -5s$  to  $-1s$ , 8 or 4 imaging frames) and the  $\Delta F/F$  of the first time point (at  $t = -5s$ ) were subtracted from all data points for the visualization of motor-triggered responses.

For brain regional average analysis, regions were included only if there were data from at least 3 larvae. As habenula and caudal hypothalamus were not consistently sampled (see above anatomical imaging section), these two regions were not included in any regional average plots (**Figures 5b, d, h, j, Supplementary Figures 7b, d, f, h, j, l, 9, 11**). Other regions without neurons from sufficient larvae that passed the sensory and/or motor function identification criteria (see above neuronal function identification sections) were also not included in some of these plots.

### *Statistics*

In all plots, significance levels are set at  $P < 0.05$ . Significant  $P$ -values are shown in black font, while near-significant values are shown in gray font. In the imaging experiments, robust statistical power was achieved with data from 5 larvae. This was supported by the substantial number of events recorded, including 593 conjugate saccades and 1747 tail flips. Additionally, the total number of blank, appetitive and aversive trials used in statistical analyses were 28, 52 and 53 respectively.

For comparisons of time spent in the different quadrants in the valence determination assay (**Figure 1c**, **Supplementary Figures 1b, c**), two-sided Z-test with population standard deviation estimated from the sample standard deviation in the control group (i.e., water only in all quadrants) was used, followed by Benjamini-Hochberg procedure to control the false discovery rate across multiple comparisons. The comparisons were made across 7 cases, including mean of individual, any 2, or all 3 chemical quadrants vs. mean of quadrant I. The most significant or near-significant *P*-values for each chemical are shown. In behavioral analysis, a two-sided Wilcoxon signed-rank test was used to assess whether the population median is zero (**Figures 3a-d, Supplementary Figures 5a-d, h-k, o-r**). Two-sided Wilcoxon rank-sum test was used to compare two sample sets (**Figures 2b, c, 3e, f, n-q, Supplementary Figures 4b, e**). For assessing expected proportions, two-sided binomial test was used (**Figures 3g-i, Supplementary Figures 4c, 5e-g, l-n, s-u**). One-sided Chi-squared test was used in comparing proportions between two groups (**Figure 3k, Supplementary Figure 4d**). For multiple group comparisons, Kruskal-Wallis test with Dunn-Sidak post hoc test was used (**Figures 4b-h, Supplementary Figures 6a-c**). Eta squared ( $\eta^2$ ) is provided as a measure of effect size. For correlation analysis, either Spearman's rank correlation (**Figures 3l, m, Supplementary Figures 3d, e**) or Pearson's correlation (**Figures 4i-m, Supplementary Figures 6d-j**) was used.

For comparisons in motor and valence preference, as well as the norm of motor and valence mutual information difference between the pallium and other brain regions, one-sided *t*-test was used (**Figures 5b, d, h, j**). Two-sided *t*-test was used to compare the mean positive valence mutual information between the pallium and the subpallium (**Supplementary Figure 7b**). To assess neuronal activation onset relative to motor event (**Figures 5k, l Supplementary Figures 9-11**), right-sided Z-tests comparing pre-chemical cue-associated event neuronal activity at the two time points preceding the motor event to zero were performed. Significance was set at 2.5 standard deviations (S.D.), with S.D. estimated from spontaneous event baseline activity variability. Adjustment for multiple comparisons across time points and brain regions was made using the Benjamini-Hochberg procedure.

## Data availability

Preprocessed data necessary to replicate these results will be made available upon acceptance of the manuscript.

## Code availability

The custom code for data analysis is available on GitHub (<https://github.com/khsamuelsy/ChemoEyeTailMvmnts/>).

## References

1. Dakin, R., Fellows, T. K. & Altshuler, D. L. Visual guidance of forward flight in hummingbirds reveals control based on image features instead of pattern velocity. *Proc Natl Acad Sci USA* 113, 8849–8854 (2016).
2. Byrne, R. A., Kuba, M. J., Meisel, D. V., Griebel, U. & Mather, J. A. Octopus arm choice is strongly influenced by eye use. *Behav. Brain Res.* 172, 195–201 (2006).
3. Bianco, I. H. & Engert, F. Visuomotor transformations underlying hunting behavior in zebrafish. *Curr. Biol.* 25, 831–846 (2015).
4. Murata, A., Yamamoto, G. & Moriwaka, M. Skill of Eye-hand Coordination in Calligraphy - Difference of Skill of Hand-Eye Coordination between Expert and Novice -. *Proc. of Fifth International Workshop on Computational Intelligence & Applications* 316–319 (2009).
5. Land, M. F. Motion and vision: why animals move their eyes. *J. Comp. Physiol. A* 185, 341–352 (1999).
6. Srivastava, A., Ahmad, O. F., Pacia, C. P., Hallett, M. & Lungu, C. The Relationship between Saccades and Locomotion. *J. Mov. Disord.* 11, 93–106 (2018).
7. Wolf, S. *et al.* Sensorimotor computation underlying phototaxis in zebrafish. *Nat. Commun.* 8, 651 (2017).
8. Dowell, C. K., Lau, J. Y. N., Antinucci, P. & Bianco, I. H. Kinematically distinct saccades are used in a context-dependent manner by larval zebrafish. *Curr. Biol.* (2024) doi:10.1016/j.cub.2024.08.008.
9. Imai, T., Moore, S. T., Raphan, T. & Cohen, B. Interaction of the body, head, and eyes during walking and turning. *Exp. Brain Res.* 136, 1–18 (2001).
10. Lohnes, C. A. & Earhart, G. M. Saccadic eye movements are related to turning performance in Parkinson disease. *J Parkinsons Dis* 1, 109–118 (2011).
11. Lavian, H., Prat, O., Petrucco, L., Štih, V. & Portugues, R. The representation of visual motion and landmark position aligns with heading direction in the zebrafish interpeduncular nucleus. *BioRxiv* (2024) doi:10.1101/2024.09.25.614953.
12. Sugioka, T., Tanimoto, M. & Higashijima, S.-I. Biomechanics and neural circuits for vestibular-induced fine postural control in larval zebrafish. *Nat. Commun.* 14, 1217 (2023).
13. Ehrlich, D. E. & Schoppik, D. A primal role for the vestibular sense in the development of coordinated locomotion. *eLife* 8, (2019).
14. Semmelhack, J. L. *et al.* A dedicated visual pathway for prey detection in larval zebrafish. *eLife* 3, (2014).
15. Mearns, D. S., Donovan, J. C., Fernandes, A. M., Semmelhack, J. L. & Baier, H. Deconstructing Hunting Behavior Reveals a Tightly Coupled Stimulus-Response Loop. *Curr. Biol.* 30, 54-69.e9 (2020).
16. Ahrens, M. B. *et al.* Brain-wide neuronal dynamics during motor adaptation in zebrafish. *Nature* 485, 471–477 (2012).
17. Naumann, E. A. *et al.* From Whole-Brain Data to Functional Circuit Models: The Zebrafish Optomotor Response. *Cell* 167, 947-960.e20 (2016).
18. Baden, T. Ancestral photoreceptor diversity as the basis of visual behaviour. *Nat. Ecol. Evol.* 8, 374–386 (2024).
19. Currier, T. A. & Nagel, K. I. Multisensory control of navigation in the fruit fly. *Curr. Opin. Neurobiol.* 64, 10–16 (2020).
20. Rössler, W. Multisensory navigation and neuronal plasticity in desert ants. *Trends Neurosci.* 46, 415–417 (2023).
21. Danilovich, S. & Yovel, Y. Integrating vision and echolocation for navigation and

- perception in bats. *Sci. Adv.* 5, eaaw6503 (2019).
- 22. Radvansky, B. A., Oh, J. Y., Climer, J. R. & Dombbeck, D. A. Behavior determines the hippocampal spatial mapping of a multisensory environment. *Cell Rep.* 36, 109444 (2021).
  - 23. Davis, S. N., Zhu, Y. & Schoppik, D. Multisensory strategies for postural compensation after lateral line loss. *BioRxiv* (2024) doi:10.1101/2024.01.23.576760.
  - 24. Sy, S. K. H. *et al.* An optofluidic platform for interrogating chemosensory behavior and brainwide neural representation in larval zebrafish. *Nat. Commun.* 14, 227 (2023).
  - 25. Wakisaka, N. *et al.* An adenosine receptor for olfaction in fish. *Curr. Biol.* 27, 1437-1447.e4 (2017).
  - 26. Hussain, A. *et al.* High-affinity olfactory receptor for the death-associated odor cadaverine. *Proc Natl Acad Sci USA* 110, 19579–19584 (2013).
  - 27. Diaz-Verdugo, C., Sun, G. J., Fawcett, C. H., Zhu, P. & Fishman, M. C. Mating suppresses alarm response in zebrafish. *Curr. Biol.* 29, 2541-2546.e3 (2019).
  - 28. Yabuki, Y. *et al.* Olfactory receptor for prostaglandin F<sub>2</sub>α mediates male fish courtship behavior. *Nat. Neurosci.* 19, 897–904 (2016).
  - 29. Braubach, O. R., Wood, H.-D., Gadbois, S., Fine, A. & Croll, R. P. Olfactory conditioning in the zebrafish (*Danio rerio*). *Behav. Brain Res.* 198, 190–198 (2009).
  - 30. Frank, T., Mönig, N. R., Satou, C., Higashijima, S.-I. & Friedrich, R. W. Associative conditioning remaps odor representations and modifies inhibition in a higher olfactory brain area. *Nat. Neurosci.* 22, 1844–1856 (2019).
  - 31. Herrera, K. J., Panier, T., Guggiana-Nilo, D. & Engert, F. Larval zebrafish use olfactory detection of sodium and chloride to avoid salt water. *Curr. Biol.* 31, 782-793.e3 (2021).
  - 32. Krishnan, S. *et al.* The right dorsal habenula limits attraction to an odor in zebrafish. *Curr. Biol.* 24, 1167–1175 (2014).
  - 33. Doyle, W. I. & Meeks, J. P. Excreted steroids in vertebrate social communication. *J. Neurosci.* 38, 3377–3387 (2018).
  - 34. Kadakia, N. *et al.* Odour motion sensing enhances navigation of complex plumes. *Nature* 611, 754–761 (2022).
  - 35. Felsenberg, J., Barnstedt, O., Cognigni, P., Lin, S. & Waddell, S. Re-evaluation of learned information in *Drosophila*. *Nature* 544, 240–244 (2017).
  - 36. Qiu, Q., Wu, Y., Ma, L. & Yu, C. R. Encoding innately recognized odors via a generalized population code. *Curr. Biol.* 31, 1813-1825.e4 (2021).
  - 37. Iravani, B., Schaefer, M., Wilson, D. A., Arshamian, A. & Lundström, J. N. The human olfactory bulb processes odor valence representation and cues motor avoidance behavior. *Proc Natl Acad Sci USA* 118, (2021).
  - 38. Schroeder, C. E., Wilson, D. A., Radman, T., Scharfman, H. & Lakatos, P. Dynamics of Active Sensing and perceptual selection. *Curr. Opin. Neurobiol.* 20, 172–176 (2010).
  - 39. Yilmaz Balban, M. *et al.* Human responses to visually evoked threat. *Curr. Biol.* 31, 601-612.e3 (2021).
  - 40. Kuroda, S., Lalonde, R. L., Mansour, T. A., Mosimann, C. & Nakamura, T. Multiple embryonic sources converge to form the pectoral girdle skeleton in zebrafish. *Nat. Commun.* 15, 6313 (2024).
  - 41. Moyle, P. & Jr, J. C. *Fishes: An Introduction to Ichthyology*. 752 (Pearson, 2003).
  - 42. Ahrens, M. B., Orger, M. B., Robson, D. N., Li, J. M. & Keller, P. J. Whole-brain functional imaging at cellular resolution using light-sheet microscopy. *Nat. Methods* 10, 413–420 (2013).
  - 43. Kermen, F. *et al.* Stimulus-specific behavioral responses of zebrafish to a large range of odors exhibit individual variability. *BMC Biol.* 18, 66 (2020).
  - 44. Mathuru, A. S. *et al.* Chondroitin fragments are odorants that trigger fear behavior in

- fish. *Curr. Biol.* 22, 538–544 (2012).
- 45. Koide, T., Yabuki, Y. & Yoshihara, Y. Terminal nerve gnrh3 neurons mediate slow avoidance of carbon dioxide in larval zebrafish. *Cell Rep.* 22, 1115–1123 (2018).
  - 46. Blin, M., Valay, L., Kuratko, M., Pavie, M. & Rétaux, S. The evolution of olfactory sensitivity, preferences, and behavioral responses in Mexican cavefish is influenced by fish personality. *eLife* 12, (2024).
  - 47. Vladimirov, N. *et al.* Light-sheet functional imaging in fictively behaving zebrafish. *Nat. Methods* 11, 883–884 (2014).
  - 48. Kim, D. H. *et al.* Pan-neuronal calcium imaging with cellular resolution in freely swimming zebrafish. *Nat. Methods* 14, 1107–1114 (2017).
  - 49. Ramirez, A. D. & Aksay, E. R. F. Ramp-to-threshold dynamics in a hindbrain population controls the timing of spontaneous saccades. *Nat. Commun.* 12, 4145 (2021).
  - 50. *Anticipatory behavior in adaptive learning systems: foundations, theories, and systems.* vol. 2684 (Springer Berlin Heidelberg, 2003).
  - 51. Dunn, T. W. *et al.* Brain-wide mapping of neural activity controlling zebrafish exploratory locomotion. *eLife* 5, e12741 (2016).
  - 52. Gillis, G. B. Undulatory Locomotion in Elongate Aquatic Vertebrates: Anguilliform Swimming since Sir James Gray. *Am. Zool.* 36, 656–665 (1996).
  - 53. Carbo-Tano, M. *et al.* The mesencephalic locomotor region recruits V2a reticulospinal neurons to drive forward locomotion in larval zebrafish. *Nat. Neurosci.* 26, 1775–1790 (2023).
  - 54. Berg, E. M. *et al.* Brainstem circuits encoding start, speed, and duration of swimming in adult zebrafish. *Neuron* 111, 372–386.e4 (2023).
  - 55. Mueller, T., Dong, Z., Berberoglu, M. A. & Guo, S. The dorsal pallium in zebrafish, *Danio rerio* (Cyprinidae, Teleostei). *Brain Res.* 1381, 95–105 (2011).
  - 56. Kermen, F., Franco, L. M., Wyatt, C. & Yaksi, E. Neural circuits mediating olfactory-driven behavior in fish. *Front. Neural Circuits* 7, 62 (2013).
  - 57. Korschning, S. I. Taste and smell in zebrafish. in *The senses: A comprehensive reference* 466–492 (Elsevier, 2020). doi:10.1016/B978-0-12-809324-5.24155-2.
  - 58. Hoover, K. C. Smell with inspiration: the evolutionary significance of olfaction. *Am. J. Phys. Anthropol.* 143 Suppl 51, 63–74 (2010).
  - 59. Parker, A. *In The Blink Of An Eye: How Vision Sparked The Big Bang Of Evolution.* 336 (Basic Books, 2004).
  - 60. Brazeau, M. D. & Friedman, M. The origin and early phylogenetic history of jawed vertebrates. *Nature* 520, 490–497 (2015).
  - 61. Thelen, E. Rhythmic behavior in infancy: An ethological perspective. *Dev. Psychol.* 17, 237–257 (1981).
  - 62. Leung, L. C. *et al.* Neural signatures of sleep in zebrafish. *Nature* 571, 198–204 (2019).
  - 63. Yang, C. *et al.* A population code for spatial representation in the zebrafish telencephalon. *Nature* (2024) doi:10.1038/s41586-024-07867-2.
  - 64. Fotowat, H., Lee, C., Jun, J. J. & Maler, L. Neural activity in a hippocampus-like region of the teleost pallium is associated with active sensing and navigation. *eLife* 8, (2019).
  - 65. Veith, J. *et al.* The mechanism for directional hearing in fish. *Nature* 631, 118–124 (2024).
  - 66. Hernandez, R. E., Galitan, L., Cameron, J., Goodwin, N. & Ramakrishnan, L. Delay of initial feeding of zebrafish larvae until 8 days postfertilization has no impact on survival or growth through the juvenile stage. *Zebrafish* 15, 515–518 (2018).
  - 67. Christou, M., Kavaliauskis, A., Ropstad, E. & Fraser, T. W. K. DMSO effects larval zebrafish (*Danio rerio*) behavior, with additive and interaction effects when combined with positive controls. *Sci. Total Environ.* 709, 134490 (2020).

68. Rhodes, M. *Introduction to Particle Technology*. (1989).
69. Randlett, O. *et al.* Whole-brain activity mapping onto a zebrafish brain atlas. *Nat. Methods* 12, 1039–1046 (2015).
70. Fehrenbach, J., Weiss, P. & Lorenzo, C. Variational algorithms to remove stationary noise: applications to microscopy imaging. *IEEE Trans. Image Process.* 21, 4420–4430 (2012).
71. Pnevmatikakis, E. A. & Giovannucci, A. NoRMCorre: An online algorithm for piecewise rigid motion correction of calcium imaging data. *J. Neurosci. Methods* 291, 83–94 (2017).
72. Giovannucci, A. *et al.* CaImAn an open source tool for scalable calcium imaging data analysis. *eLife* 8, (2019).
73. Moon, Y. I., Rajagopalan, B. & Lall, U. Estimation of mutual information using kernel density estimators. *Phys. Rev. E Stat. Phys. Plasmas Fluids Relat. Interdiscip. Topics* 52, 2318–2321 (1995).

## Acknowledgement

We thank Dorothy Ieong for zebrafish husbandry and technical support, and Anki Miu for administrative assistance for the project. We thank Hui Zhao and Shen Gu for the provision of zebrafish larvae for equipment testing during initial protocol establishment. This work was supported by a Croucher Innovation Award (CIA20CU01) from the Croucher Foundation; the General Research Fund (14100122), the Collaborative Research Fund (C6027-19GF, C7074-21GF and C4062-22EF), and the Area of Excellence Scheme (AoE/M-604/16) of the RGC of UGC of Hong Kong; the Health@InnoHK program of the Innovation and Technology Commission of Hong Kong; the Excellent Young Scientists Fund (Hong Kong and Macau) (82122001) from the National Natural Science Foundation of China; the Asian Young Scientist Fellowship from the Future Science Awards Foundation; Margaret K. L. Cheung Research Centre for Management of Parkinsonism; the Lo's Family Charity Fund Limited.

## Author contributions

Conceptualization: S.K.H.S., H.K.

Methodology: S.K.H.S., C.F., K.W., Y.M., O.R., Y.H., H.K.

Investigation: S.K.H.S., D.C.W.C., J.J.Z., J.L., C.F., Y.H., H.K.

Data Curation: S.K.H.S.

Formal Analysis: S.K.H.S.

Software: S.K.H.S., H.K.

Validation: S.K.H.S., H.K.

Visualization: S.K.H.S.

Supervision: H.K.

Project Administration: S.K.H.S., V.C.T.M., K.K.Y.W., H.K.

Funding Acquisition: V.C.T.M., K.K.Y.W., H.K.

Writing - Original Draft: S.K.H.S., D.C.W.C., H.K.

Writing - Review & Editing: All authors.

## Competing interests

The authors declare no competing interests.

**Figure 1**

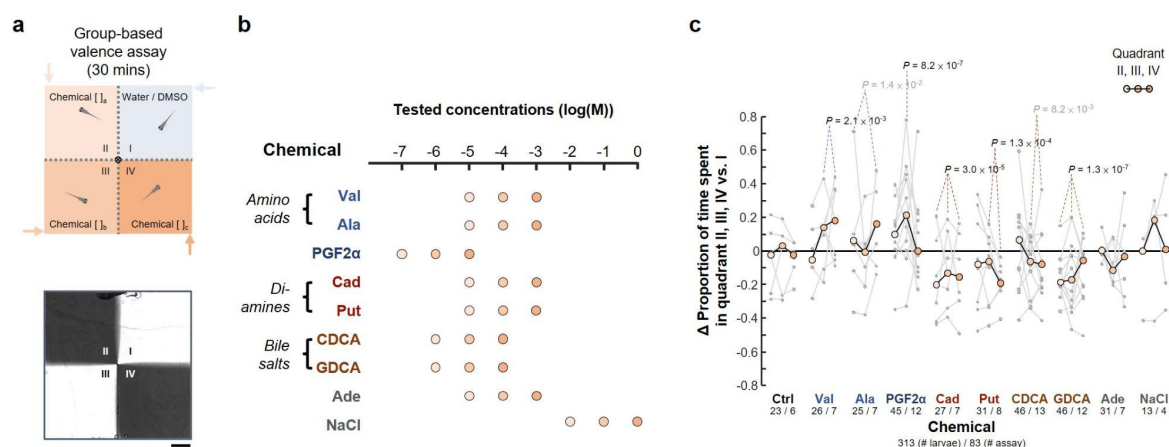


**Figure 1. A fluidics-based chemical valence determination assay.** (a) Upper panel: Schematic of the assay. Zebrafish larvae swimming in a two-dimensional arena (40 mm × 40 mm × 1.5 mm) are imaged at 20 fps under infrared (IR) illumination in the absence of visible light (see **Supplementary Figure 1a** for a more detailed schematic for the setup). Four quadrants with equal area are created and maintained by a constant, slow inflow of fluid at each corner (marked by arrows), with outflow occurring at a shared central outlet. The laminar flow maintains static borders between the zones. Lower panel: Visualization of the well-defined quadrants by infusing IR dyes into quadrant II and IV, and water into quadrant I and III. Scale bar: 5 mm. (b) Assayed chemicals and tested concentrations (varied across 3 consecutive orders of magnitude for each), including valine (Val), alanine (Ala), prostaglandin F2 $\alpha$  (PGF2 $\alpha$ ), cadaverine (Cad), putrescine (Put), chenodeoxycholic acid (CDCA), glycodeoxycholic acid (GDCA), adenosine (Ade), and sodium chloride (NaCl). These were dissolved either in water or 0.5% DMSO and infused into quadrant II (lowest concentration) to IV (highest concentration). (c) Differences in time spent in the chemical quadrants (i.e., II–IV, with different and increasing concentrations for each of the tested chemicals as indicated in (b) compared with the control quadrant (i.e., I), showing the values of individual assays (gray) and the medians (black). Below each chemical name, the first number indicates the total number of larvae assayed, and the second number specifies the total number of assays performed. *P*-values: Multiple Z-tests comparing different quadrant combinations' means to zero, with population standard deviation (S.D.) estimated from the sample S.D. of the control group (see **Methods**). Statistical significance after Benjamini-Hochberg adjustment: Black, significant; gray, near-significant.

**Figure 2**

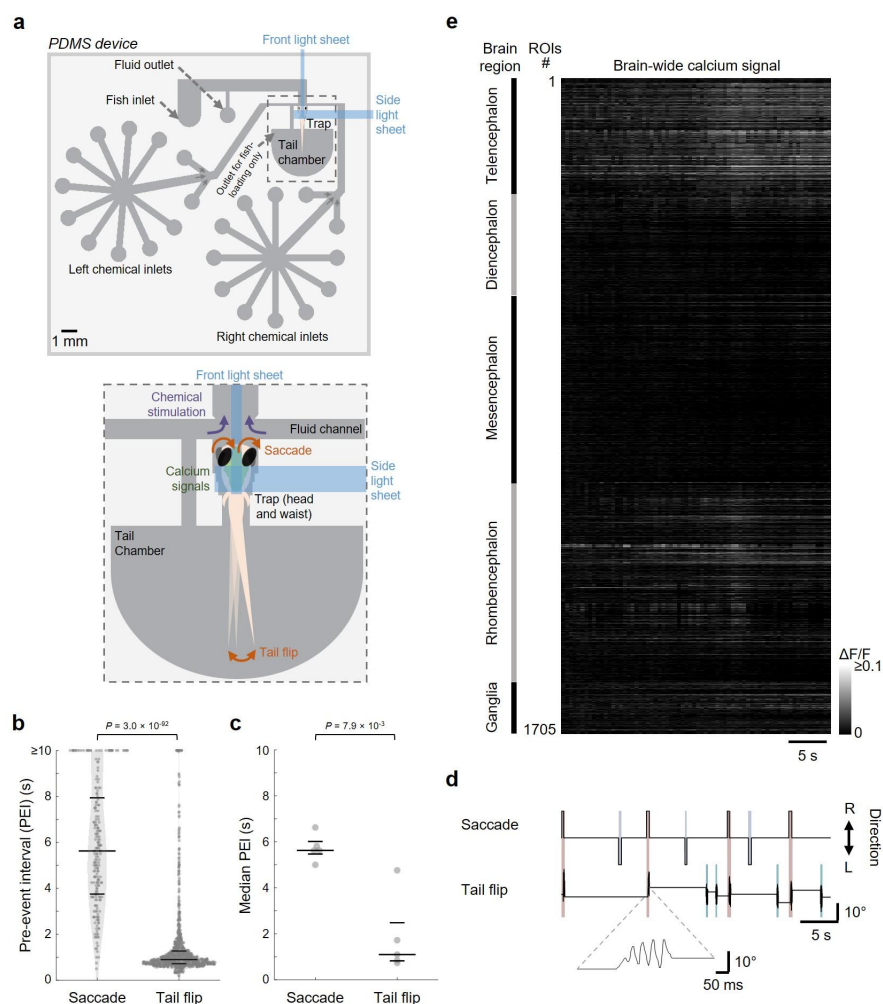


**Figure 2. An optimized optofluidic imaging device for recording of brain-wide chemosensory cue-elicited neural activity, saccadic eye and tail flip movements.** (a) Upper panel: A drawing of the enhanced polydimethylsiloxane (PDMS)-based microfluidic device, featuring multiple chemical delivery channels on both sides of the larval head chamber. These channels are offset from the front to accommodate front excitation light sheet scanning, in addition to the right side light sheet. Lower panel: A close-up illustration of the neural-behavioral imaging capabilities in a larval subject during precisely controlled chemical stimulus presentation. (b) & (c) Pre-event intervals (PEIs) of spontaneous saccade and tail flip, showing values for (b) all recorded events and (c) the median of each larva. Horizontal lines show the median, 25<sup>th</sup> and 75<sup>th</sup> percentiles for each plot.  $n = 5$  larvae with 216 spontaneous saccades and 1018 spontaneous tail flips, each with a recorded preceding reference event. In (b), shaded areas scale according to the probability density function of values.  $P$ -values: Two-sided Wilcoxon rank-sum test. (d) An example showing spontaneous saccades and tail flips of a larval subject, with a zoom-in example tail flip shown below. Temporally coupled saccades and tail flips ( $\leq 0.5$ s onset time difference) are indicated with coral blocks. Other saccades and tail flips are highlighted with blue and teal blocks, respectively. (e) Heatmap of brain-wide spontaneous neuronal activities simultaneously acquired with motor outputs shown in (d).

**Figure 3**

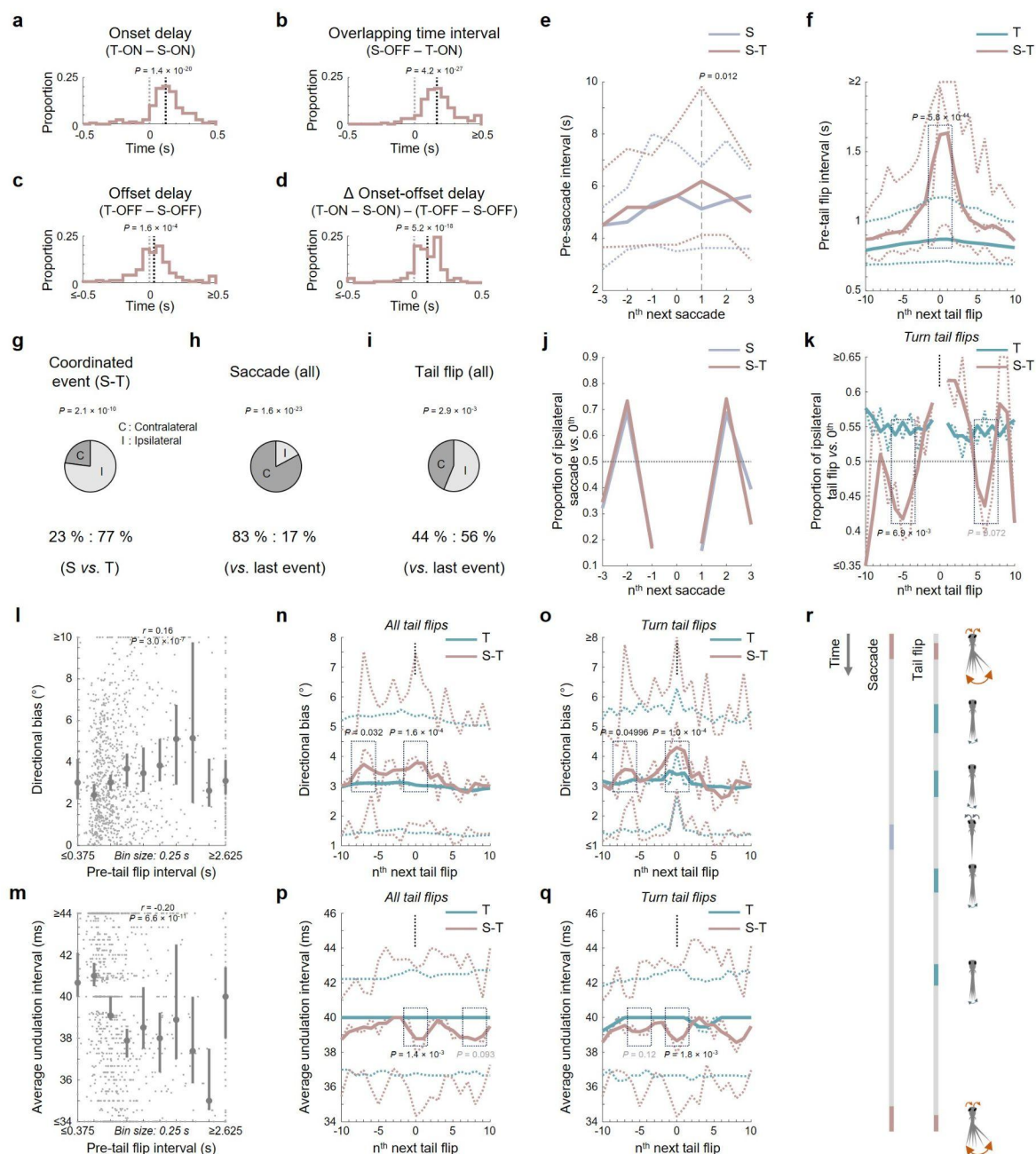


**Figure 3. Properties of spontaneous coordinated saccade-tail flips.** (a)–(d) Histograms showing (a) onset delay, (b) overlapping time interval, (c) offset delay and (d) difference in onset-offset delay of coupled saccade-tail flip (S-T) events (also see **Supplementary Figure 3a** for illustration of these temporal parameters). Note that the precision of measurements for the onset and offset for saccade and tail flip were 0.0625s and 0.0025s due to the respective sampling rates. Black and gray dashed lines indicate median and zero respectively. *P*-values: Two-sided Wilcoxon signed-rank test. (e) & (f) Pre-event intervals of self and flanking (e) saccades and (f) tail flips with respect to independent (S, saccade; T, tail flip) or S-T events. (g)–(i) Pie charts showing the proportions of contra- and ipsilateral turns, comparing the directionality of (g) saccades (S) and tail flips (T; only turns considered, see **Methods**) in S-T events, (h) saccades and their preceding events, and (i) tail flips and their preceding events. *P*-values: Two-sided binomial test. (j) & (k) Proportions of ipsilateral turns in flanking (j) saccades and (k) turn tail flips (directional bias  $\geq 1.5^\circ$ ) with respect to independent (S, T) or S-T events. In (k), the raw proportions (thin lines) and corresponding moving-average curves (thick lines) are shown. *P*-value: One-sided Chi-squared test. (l) & (m) Medians and 95% confidence intervals (based on bootstrapping with 1000 resamples) of the (l) directional bias and (m) average undulation interval of all tail flips vs. their pre-tail flip interval (binned). Gray dots are individual data points. Spearman's rank correlation coefficients (*r*) and associated *P*-values are shown. (n) & (o) Directional bias of self and flanking [(n) all and (o) turn] tail flips with respect to independent tail flips (T) or S-T events. (p) & (q) Average undulation interval of self and flanking [(p) all and (q) non-turn] tail flips with respect to independent tail flips (T) or S-T events. (r) Illustration of the temporal, directional and kinematic coordination of spontaneous saccades and tail flips. Abbreviations in (a)–(d), ON, onset; OFF, offset. In (e), (f), (n)–(q), the thin curves represent the medians, 75<sup>th</sup> and 25<sup>th</sup> percentiles of all events. The raw median values (thin lines) and corresponding moving-average curves (thick lines) are shown in all these plots except (e). *P*-values: Two-sided Wilcoxon rank-sum test. For all plots, data were collected from  $n = 5$  larvae, with 330 spontaneous saccades and 1116 spontaneous tail flips.

**Figure 4**

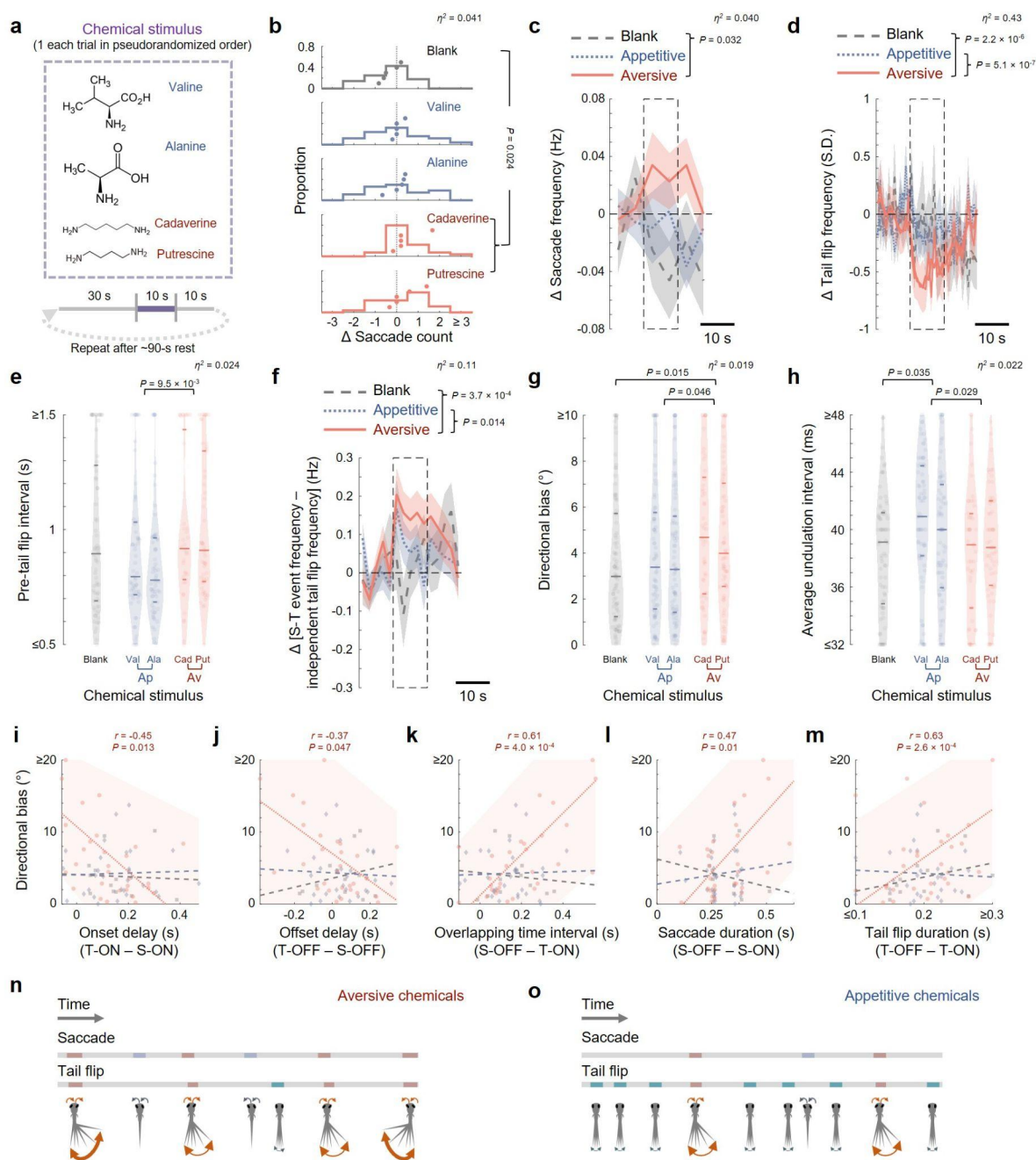


**Figure 4. Behavioral effects of chemosensory cues on saccade and tail flip.** **(a)** Illustration of chemical stimulation paradigm. During each trial, one appetitive or aversive chemical was administered to a tethered larval subject under neural-behavioral imaging. **(b)** Histograms showing the distributions of difference in saccade count between the 10-second stimulus window and the 10-second pre-stimulus period, across trials for each chemical and blank control. Each dot represents a trial-averaged saccade count change from a larva (dispersed vertically for visualization). **(c)** & **(d)** Stimulus-evoked changes in **(c)** saccade frequency and **(d)** normalized tail flip frequency (see **Methods**), compared with the pre-stimulus average. **(e)** Pre-tail flip interval of chemical stimuli-associated tail flips. **(f)** Stimulus-associated changes in the relative frequency of coupled saccade-tail flip (S-T) events vs. all tail flips (i.e.,  $\Delta[\text{S-T event frequency} - \text{independent tail flip frequency}]$ ) across time. **(g)** & **(h)** Kinematic parameters of chemical stimuli-associated tail flips including **(g)** directional bias (all tail flips) and **(h)** average undulation interval (for tail flips with  $\geq 4$  undulation cycles). **(i)**–**(m)** Scatter plots of directional bias vs. various temporal parameters for S-T events, including saccade-tail flip **(i)** onset delay, **(j)** offset delay, **(k)** overlapping time interval, **(l)** saccade duration, and **(m)** tail flip duration. Individual data points are shown in squares, diamonds and circles for the blank, appetitive and aversive groups respectively. **(n)** & **(o)** Illustrations of larval zebrafish behavioral changes upon **(n)** aversive and **(o)** appetitive chemicals presentations. In **(c)**, **(d)**, and **(f)**, quantities are binned and normalized to the average values in the 10-second pre-stimulus windows (see **Methods**). Lines and shadows show mean  $\pm$  SEM (across trials). In **(d)**, the raw means (thin lines) and corresponding moving-average curves (thick lines) are shown. Dashed rectangles mark the stimulus window. In **(e)**, **(g)** and **(h)**, horizontal lines indicate medians, 75<sup>th</sup> and 25<sup>th</sup> percentiles. Shadows of the violin plots scale according to the probability density function. In **(b)**–**(h)**, *P*-values: Kruskal–Wallis test with Dunn-Sidak post hoc test. Eta squared ( $\eta^2$ ) is provided as a measure of effect size. In **(i)**–**(m)**, lines show best linear fits of each data group and shadows show 95% prediction confidence intervals of the aversive chemical data group (the only that exhibited significant associations). Pearson’s correlation coefficients (*r*) and associated *P*-values are shown for the aversive chemical data points. Only data points with saccade onset certainly earlier than the tail flip onset were included in the regression analysis (see **Methods**). In **(l)**, saccade duration values (sampled at a temporal resolution of 0.125s) are slightly horizontally dispersed for visualization. Abbreviations: S, saccade; T, tail flip; ON, onset; OFF, offset; Ap, appetitive; Av, aversive. For all plots, data were collected from *n* = 5 larvae, and the total numbers of blank control, appetitive and aversive chemical trials used in statistical analyses are 28, 52 and 53, respectively. In **(d)**, the numbers of blank, appetitive and aversive trials with non-zero pre-stimulus tail flip frequency used in statistical analyses are 19, 34 and 27, respectively. In **(e)**, the total numbers of blank, appetitive and aversive events used in statistical analyses are 69, 130 and 89, respectively. In **(g)**, the total numbers of blank, appetitive and aversive events used in statistical analyses are 89, 167 and 124, respectively. In **(h)**, the total numbers of blank, appetitive and aversive events used in statistical analyses are 76, 156 and 111, respectively.

**Figure 5**

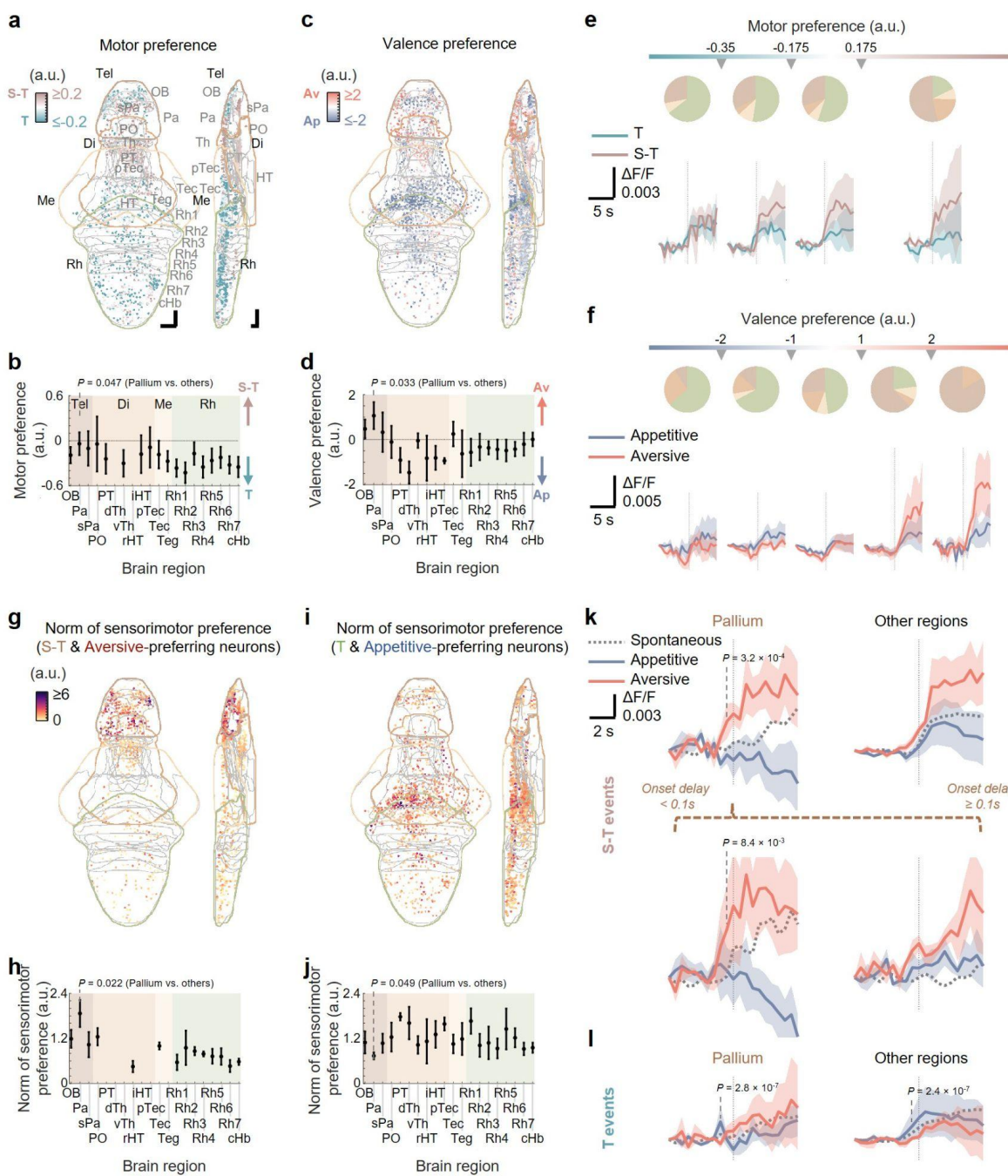
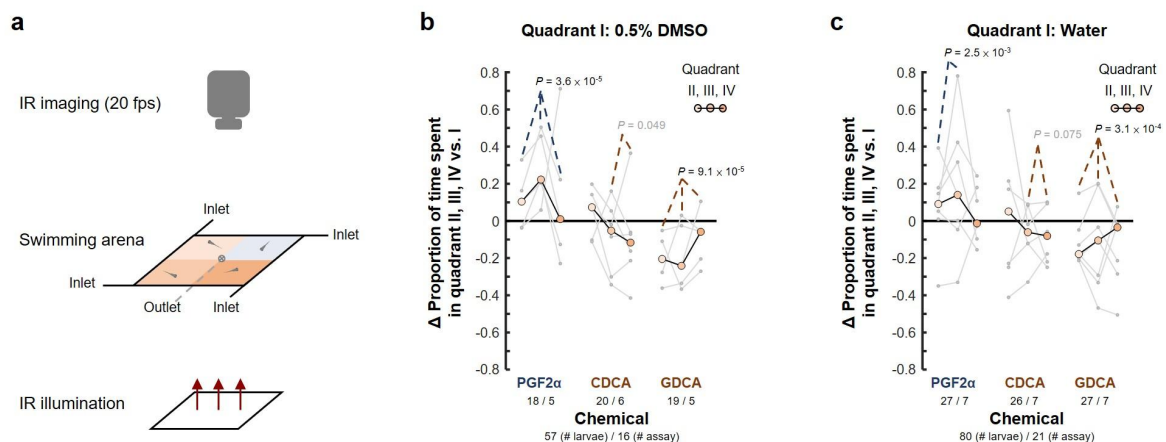


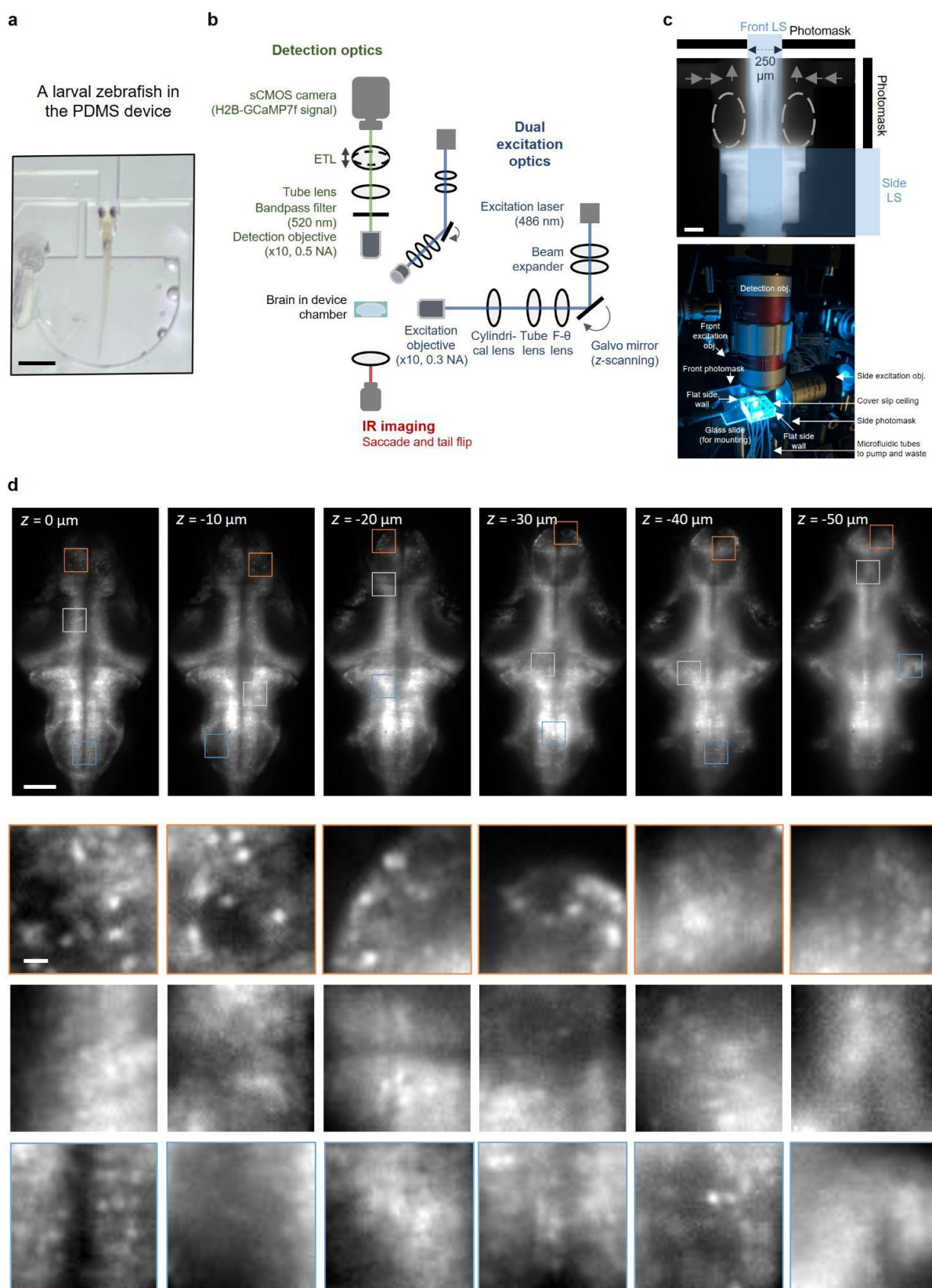
**Figure 5. Neuronal basis underlying chemosensory-driven eye-body coordination.** **(a)** Mean intensity projections (to transverse and sagittal planes) of motor preference of motor-encoding regions-of-interest (ROIs) (see **Methods**). **(b)** Regional mean  $\pm$  S.E.M. (across larvae) of motor preference. **(c)** Mean intensity projects (to transverse and sagittal planes) of valence preference for all valence-encoding ROIs (see **Methods**). **(d)** Regional mean  $\pm$  S.E.M. (across larvae) of valence preference. **(e)** Upper panel: Pie charts showing median regional distributions of ROIs (across larvae) with motor preference in different ranges. Lower panel: Mean  $\pm$  S.E.M. (across larvae) responses of motor-encoding ROIs with motor preference in different ranges. Dotted vertical lines indicate the times of tail flip onsets (in a corresponding neuronal imaging frame). **(f)** Upper panel: Pie charts showing median regional distributions of ROIs (across larvae) with valence preference in different ranges. Lower panel: Mean  $\pm$  S.E.M. (across larvae) responses of valence-encoding ROIs with valence preference in different ranges. Dotted vertical lines indicate the time points of stimulus onsets (between two neuronal imaging frames). **(g)** Mean intensity projections (to transverse and sagittal planes) of norm of sensorimotor preference (see **Methods**), for all ROIs preferring S-T event and aversive valence (quadrant I in **Supplementary Figure 8a**, also see **Supplementary Figure 8b** for zoom-in of the forebrain area). **(h)** Regional mean  $\pm$  S.E.M. (across larvae) of norm of sensorimotor preference for all ROIs preferring S-T event and aversive valence. **(i)** Mean intensity projections (to transverse and sagittal planes) of norm of sensorimotor preference for all ROIs preferring independent tail flip and appetitive valence (quadrant III in **Supplementary Figure 8a**, also see **Supplementary Figure 8c** for zoom-in of the forebrain area). **(j)** Regional mean  $\pm$  S.E.M. (across larvae) of norm of sensorimotor preference, for all ROIs preferring independent tail flip and appetitive valence. **(k)** Upper panel: Mean  $\pm$  S.E.M. (across larvae) responses of motor-encoding ROIs in the pallium (left) and non-pallial brain regions (right) to chemical cue-associated saccade-coupled tail flips. Lower panel: Mean  $\pm$  S.E.M. (across larvae) responses of motor-encoding ROIs in the pallium to chemosensory cue-associated saccade-coupled tail flips with saccade-tail flip onset delay  $< 0.1$  seconds (left) or  $\geq 0.1$  seconds (right). **(l)** Mean  $\pm$  S.E.M. (across larvae) responses of motor-encoding ROIs in the pallium (left) and non-pallial brain regions (right) to chemical cue-associated independent tail flips. In **(k)** & **(l)**, dotted traces show the corresponding neuronal responses of spontaneous events. Dotted vertical lines indicate the time points of tail flip onsets (in a corresponding neuronal imaging frame). Scale bars in **(a)**: 50  $\mu$ m in the Z-Brain Atlas space. In **(b)**, **(d)**, and **(h)**, *P*-values: Right-sided *t*-test comparing the pallium and non-pallial brain regions. In **(j)**, *P*-value: Left-sided *t*-test comparing the pallium and non-pallial brain regions. In **(k)** & **(l)**, *P*-values: Right-sided *Z*-tests comparing pre-chemical cue-associated event neuronal activity at each time point to zero. Significance was set at 2.5 standard deviations (S.D.), with S.D. estimated from spontaneous event baseline activity variability. Adjustment for multiple comparisons across time points and brain regions was made using the Benjamini-Hochberg procedure (see **Methods**). In **(a)**–**(j)**, the major brain regions (telencephalon, diencephalon, mesencephalon and rhombencephalon) are color-coded. Abbreviations of brain regions: OB olfactory bulb, Pa pallium, sPa subpallium, PO preoptic area, PT posterior tuberculum, dTh dorsal thalamus, vTh ventral thalamus, rHT rostral hypothalamus, iHT intermediate hypothalamus, pTec pretectum, Teg tegmentum, Rh1 rhombomere 1, Rh2 rhombomere 2, Rh3 rhombomere 3, Rh4 rhombomere 4, Rh5 rhombomere 5, Rh6 rhombomere 6, Rh7 rhombomere 7, cHb caudal hindbrain. Other abbreviations: S-T, coupled saccade-tail flip; T, independent tail flip: Ap, appetitive; Av, aversive. For all plots, the neural activity data correspond to the behavioral data reported in **Figures 3 & 4**, collected from  $n = 5$  larvae.

## Supplementary Figure 1



**Supplementary Figure 1. Schematic of setup and comparisons of valence determination assays results using 0.5% DMSO vs. water as control.** **(a)** Schematic of the valence determination assay. Zebrafish larvae swimming in a two-dimensional arena ( $40\text{ mm} \times 40\text{ mm} \times 1.5\text{ mm}$ ) are imaged at 20 fps under infrared (IR) illumination in the absence of visible light. Four quadrants with equal area are created and maintained by a constant, slow inflow of fluid at each corner, with outflow at a shared central outlet. The laminar flow maintains static borders between the zones. **(b)** & **(c)** Differences in time spent in the chemical quadrants (i.e., II–IV, with different and increasing concentrations for each of the tested chemicals as indicated in **Figure 1b**) compared with the water quadrant (i.e., I), showing the values of individual assays (gray) and the medians (black). The experiments were performed with either **(b)** 0.5% DMSO or **(c)** water in quadrant I. Below each chemical name, the first number indicates the total number of larvae assayed, and the second number specifies the total number of assays performed.  $P$ -values: multiple Z-tests across different quadrant combinations' means to zero, with population standard deviation (S.D.) estimated from the sample S.D. of the control group (see **Methods**). Statistical significance after Benjamini-Hochberg adjustment: Black, significant; gray, near-significant.

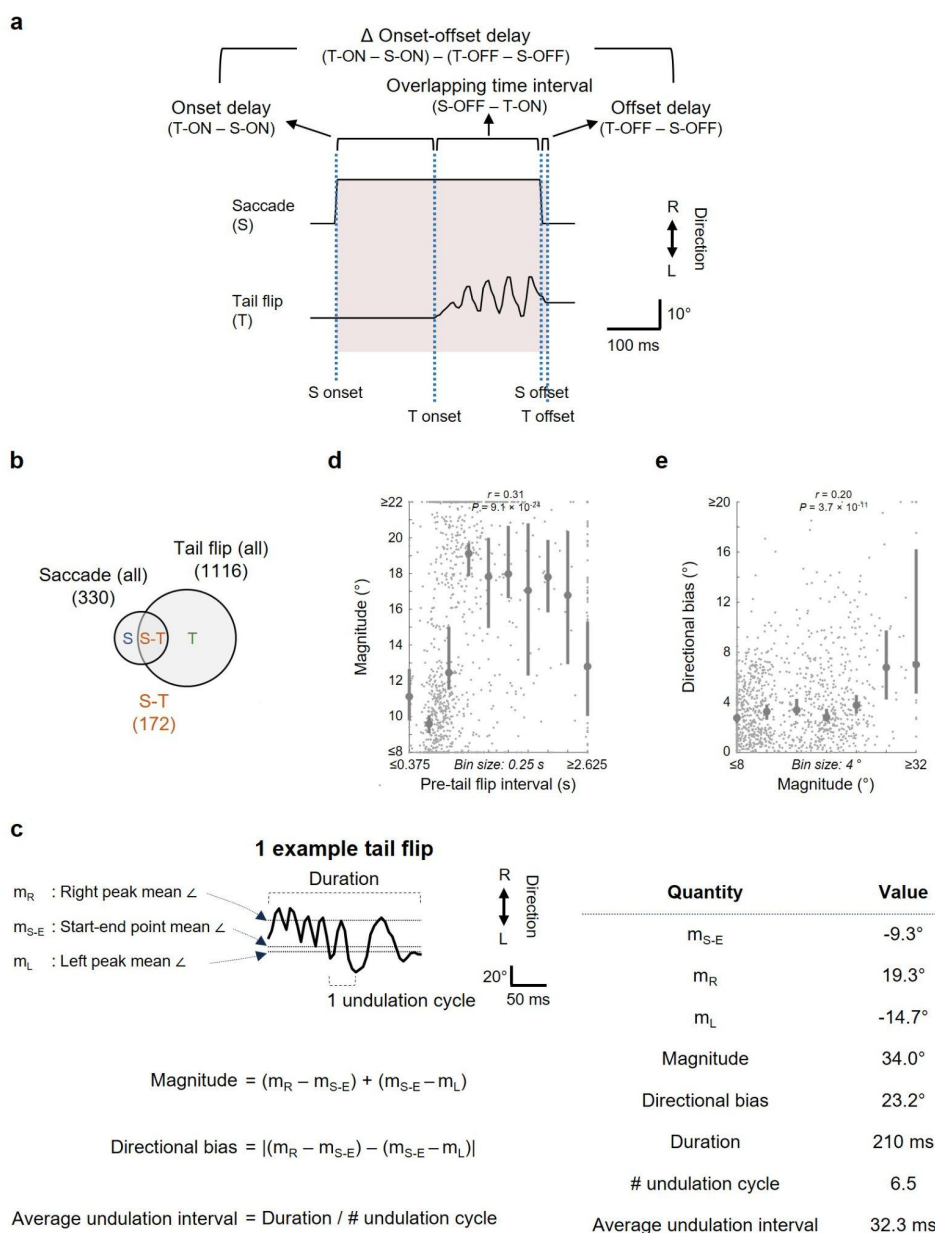
## Supplementary Figure 2



**Supplementary Figure 2. Additional data on the improved imaging device for recording of brain-wide chemosensory cue-associated neural activity, saccade and tail movements.**

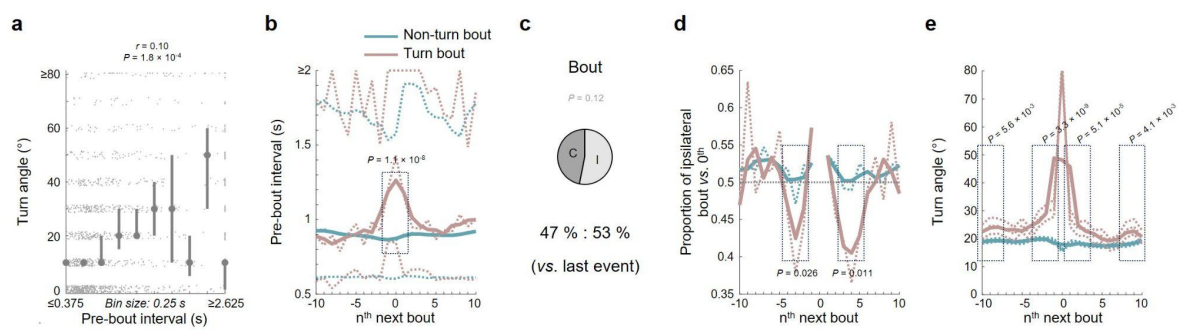
**(a)** A photograph of a tethered larval zebrafish loaded into a PDMS-based microfluidic device (scale bar: 1 mm). Its eyes and tail are free to move while the head is fixed in place for fluorescence imaging. **(b)** Optical layout of the light sheet microscope, including two light sheet scanning modules which scan the larval brain from the side and the front respectively, a fluorescence detection module, and an infrared (IR) imaging module for saccade and tail movement recordings. **(c)** Upper panel: A fluorescence image showing sodium fluorescein in the microfluidic device excited by the front and side scanning light sheets (LS, illustrated by overlaid blue shadows), with photomasks placed to avoid the light sheets from directly reaching the larval eye positions (marked with white dashed ovals). A 250- $\mu$ m window in the front photomask allows for the passage of the front excitation light to scan the brain regions between the eyes. Scale bar: 100  $\mu$ m. Lower panel: A photograph showing the microfluidic device, objectives, and the associated tubings. **(d)** Upper panel: Six example planes of imaging a larval zebrafish brain expressing H2B-GCaMP7f in neurons (scale bar: 100  $\mu$ m). Lower panel: Zoom-in images of the corresponding planes which show population of individual neurons (scale bar: 10  $\mu$ m). Images are contrast-adjusted for display.

### Supplementary Figure 3



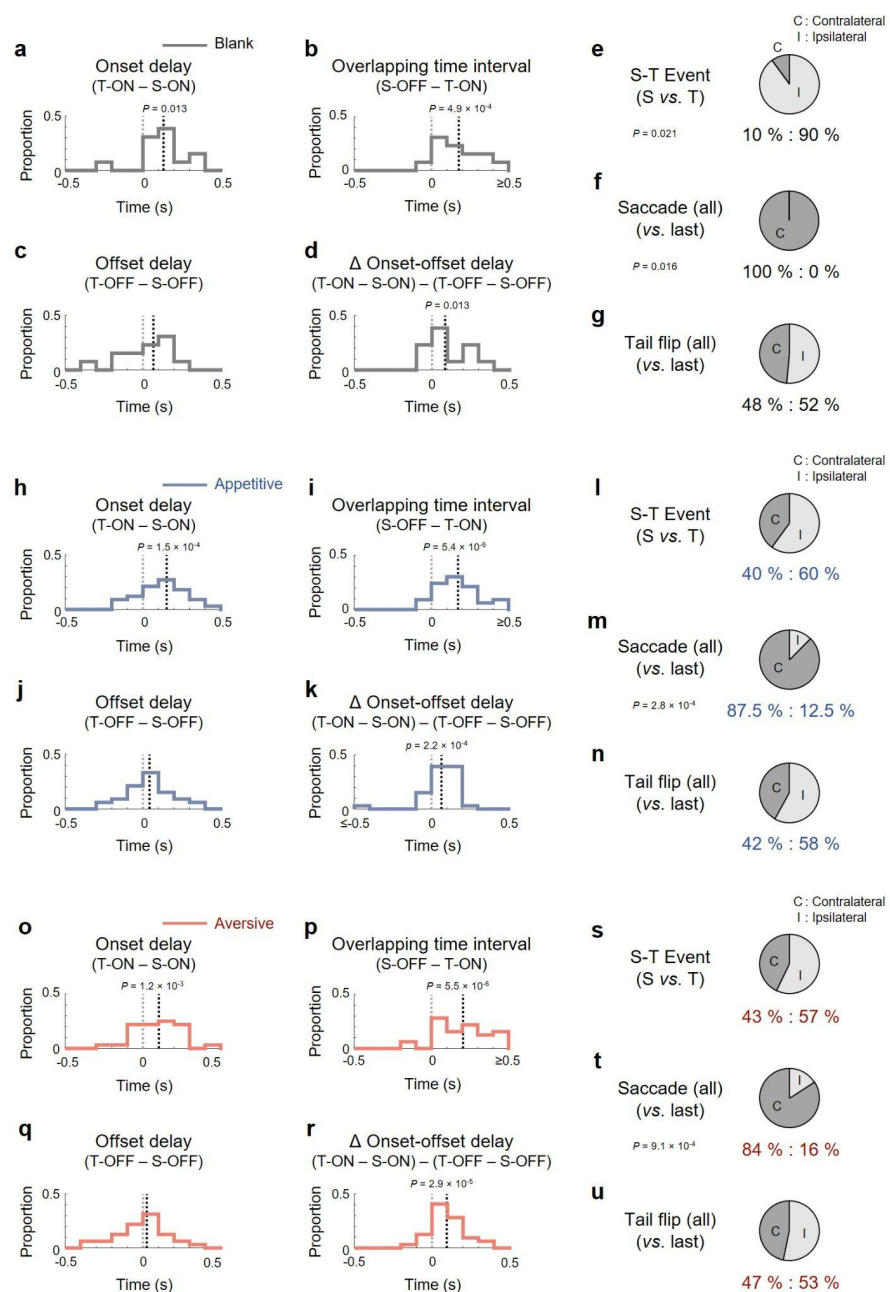
**Supplementary Figure 3. Additional analysis of spontaneous saccade-tail flip coordination.** (a) Schematic illustrating the various temporal parameters of a coupled saccade-tail flip (S-T) event from **Figure 2d**. (b) Venn diagram showing all counts of spontaneous saccades, tail flips and S-T events ( $n = 5$  larvae). (c) Illustration of the underlying calculation for the various kinematic parameters of an example tail flip. Dashed lines indicate the right peak mean angle, start-end point mean angle, and left peak mean angle. (d) Medians and the 95% confidence intervals (based on bootstrapping with 1000 resamples) of the magnitude of all tail flips vs. their pre-tail flip intervals (binned). (e) Medians and the 95% confidence intervals (based on bootstrapping with 1000 resamples) of the directional bias of all tail flips vs. their magnitudes (binned). In (d) & (e), gray dots are individual data points. Spearman's rank correlation coefficients ( $r$ ) and associated  $P$ -values are shown.

## Supplementary Figure 4



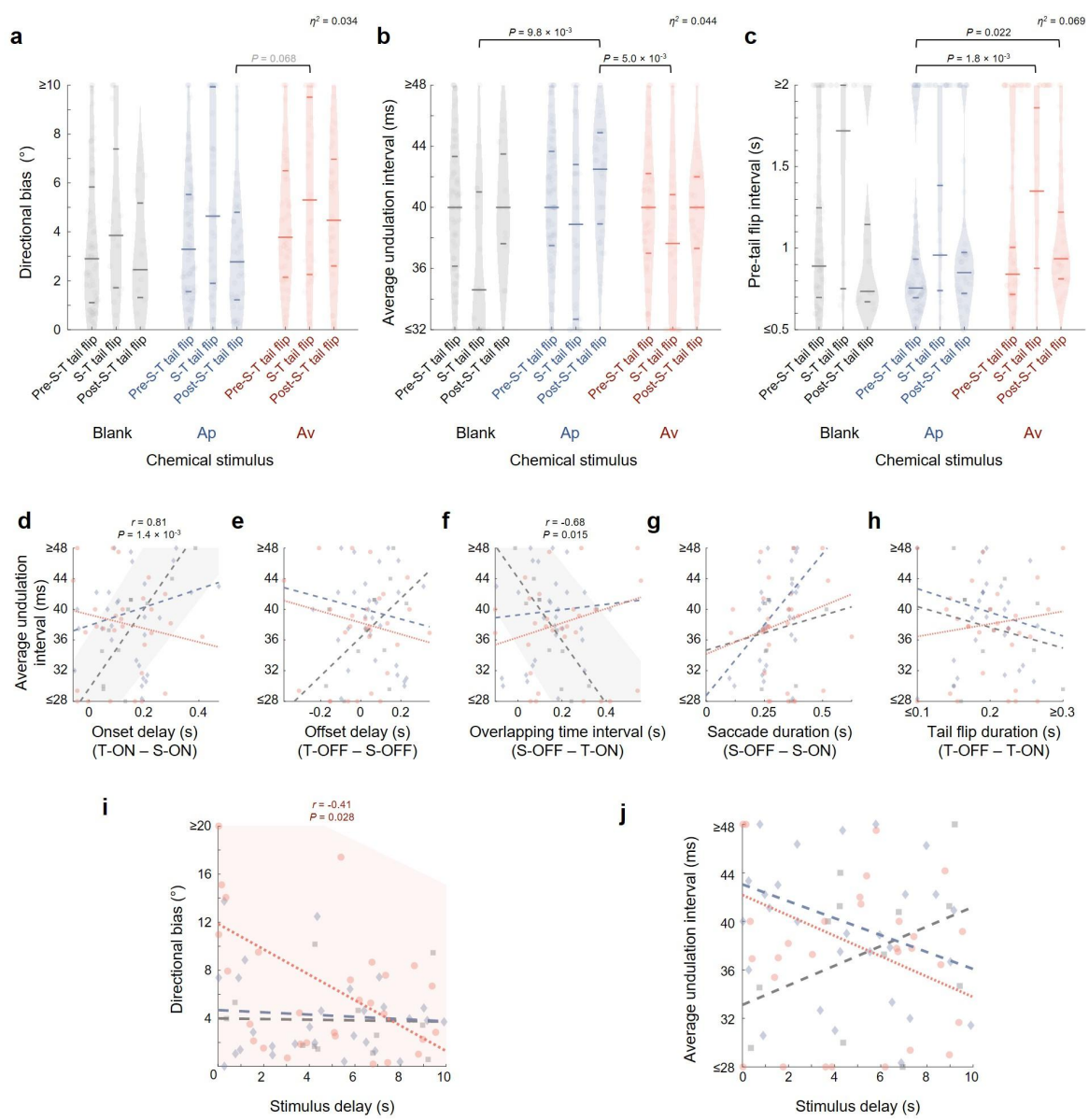
**Supplementary Figure 4. Kinematic analysis based on data from zebrafish larvae freely swimming in water.** (a) Medians and the 95% confidence intervals (based on bootstrapping with 1000 resamples) of the turn angle of all swim bouts vs. their pre-bout intervals (binned). Gray dots are individual data points. Turn angle values (sampled at an angular resolution of 10°) are slightly vertically dispersed for visualization. Spearman's rank correlation coefficients ( $r$ ) and associated  $P$ -values are shown. (b) Pre-event intervals of self and flanking swim bouts with respect to non-turn (teal) or turn (coral) swim bouts (see **Methods**). Thin curves represent the raw median values, 75<sup>th</sup> and 25<sup>th</sup> percentiles. Thick curves are the moving-average of medians. (c) Pie chart showing the proportions of contra- and ipsilateral consecutive turns (i.e., comparing each swim bout to its preceding event).  $P$ -value: Two-sided binomial test. (d) Proportion of ipsilateral turn in flanking swim bouts with respect to non-turn (teal) or turn (coral) events. The raw median values (thin lines) and corresponding moving-average curves (thick lines) are shown.  $P$ -values: One-sided Chi-squared test. (e) Turn angle of self and flanking tail flips with respect to non-turn (teal) or turn (coral) swim bouts. The thin curves represent mean  $\pm$  S.E.M. across time. The raw (thin lines) and corresponding moving-average curves (thick lines) for the mean are shown. In (b) & (e),  $P$ -values: Two-sided Wilcoxon rank-sum test. Note that in (e), the centered bout (i.e., 0<sup>th</sup> next bout) is by definition different and therefore only flanking bouts are compared. For all plots, data were collected from  $n = 11$  larvae, with 1,529 spontaneous swim bouts.

## Supplementary Figure 5



**Supplementary Figure 5. Temporal and directional characteristics of coupled saccade-tail flip (S-T) events under chemical stimulus presentation.** (a)–(d) Histograms of saccade-tail flip (a) onset delay, (b) overlapping time interval, (c) offset delay and (d) difference in onset-offset delay of S-T events during blank stimuli. Note that the precision of measurements for the onset and offset for saccade and tail flip were 0.0625s and 0.0025s due to the respective sampling rates. Black and gray dashed lines indicate median and zero respectively. *P*-values: Two-sided Wilcoxon signed-rank test. (e)–(g) Pie charts showing the proportions of contra- and ipsilateral turns, comparing the directionality of (e) saccades and turns in S-T events, (f) saccades and their preceding events, and (g) tail flips and their preceding events. *P*-values: Two-sided binomial test. (h)–(n) and (o)–(u) are similar to (a)–(g) but showing results during appetitive and aversive chemical presentations, respectively. Abbreviations: S, saccade; T, tail flip; ON, onset; OFF, offset.

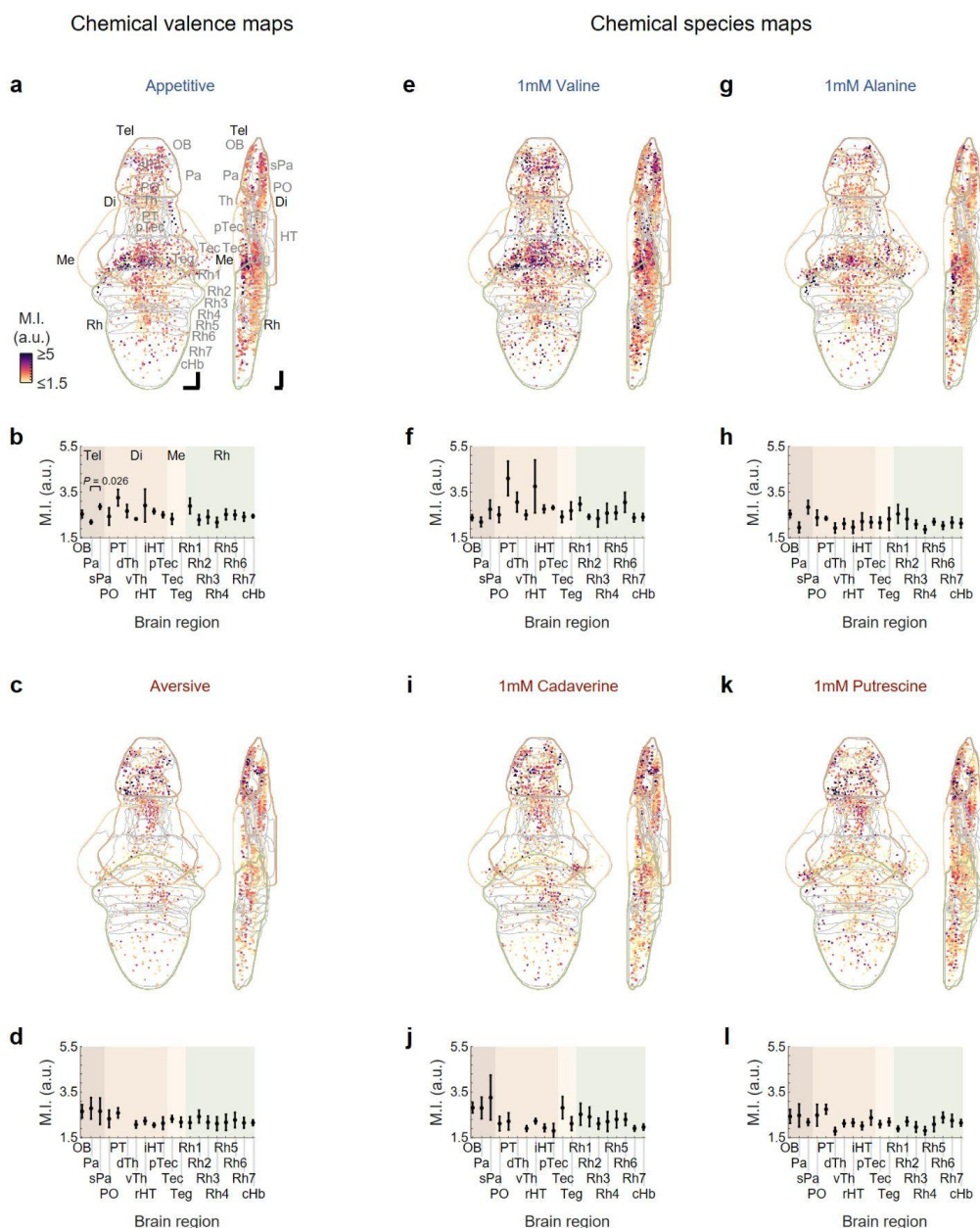
## Supplementary Figure 6



**Supplementary Figure 6. Additional kinematic and temporal analysis of spontaneous coupled saccade-tail flip (S-T) coordination during chemical presentation. (a)–(c)**

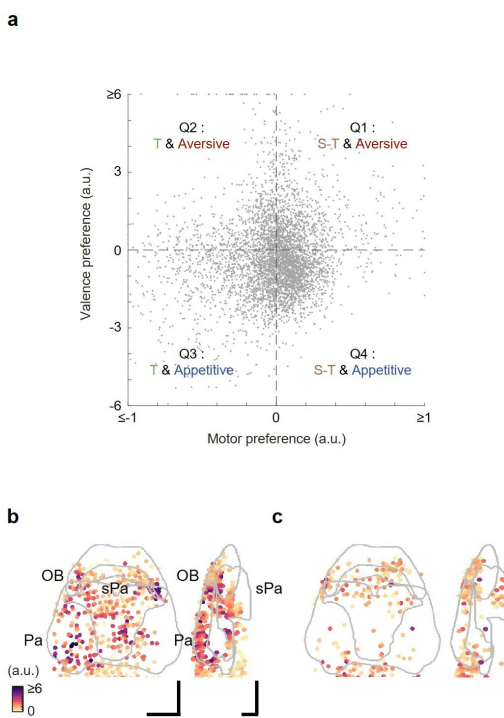
Kinematic parameters of tail flips subgrouped into chemical stimulus-associated pre-S-T (independent), S-T and post-S-T (independent) tail flips including **(a)** directional bias, **(b)** average undulation interval, and **(c)** pre-tail flip interval. Horizontal lines indicate the medians, 75<sup>th</sup> and 25<sup>th</sup> percentiles. Shadows of the violin plots scale according to the probability density function. *P*-values: Kruskal–Wallis test with Dunn–Sidak post hoc test. Eta squared ( $\eta^2$ ) is provided as a measure of effect size. Abbreviations: Ap, appetitive; Av, aversive. **(d)–(h)** Scatter plots of average undulation interval vs. various temporal parameters for S-T events, including saccade-tail flip **(d)** onset delay, **(e)** offset delay, **(f)** overlapping time interval, **(g)** saccade duration, and **(h)** tail flip duration. **(i) & (j)** Scatter plots showing **(i)** directional bias and **(j)** average undulation interval vs. stimulus delay for S-T events. In **(d)–(j)** Individual data points are shown in squares, diamonds and circles for the blank control, appetitive and aversive chemical groups respectively. Lines show best linear fits of each data group and shadows show 95% prediction confidence intervals of the blank control data group in **(d) & (f)** (the only that exhibited significant associations) and aversive chemical data group in **(i)** (the only that exhibited significant association). Pearson's correlation coefficient (*r*) and associated *P*-value are shown for the **(d) & (f)** blank control and **(i)** aversive chemical data points.

## Supplementary Figure 7



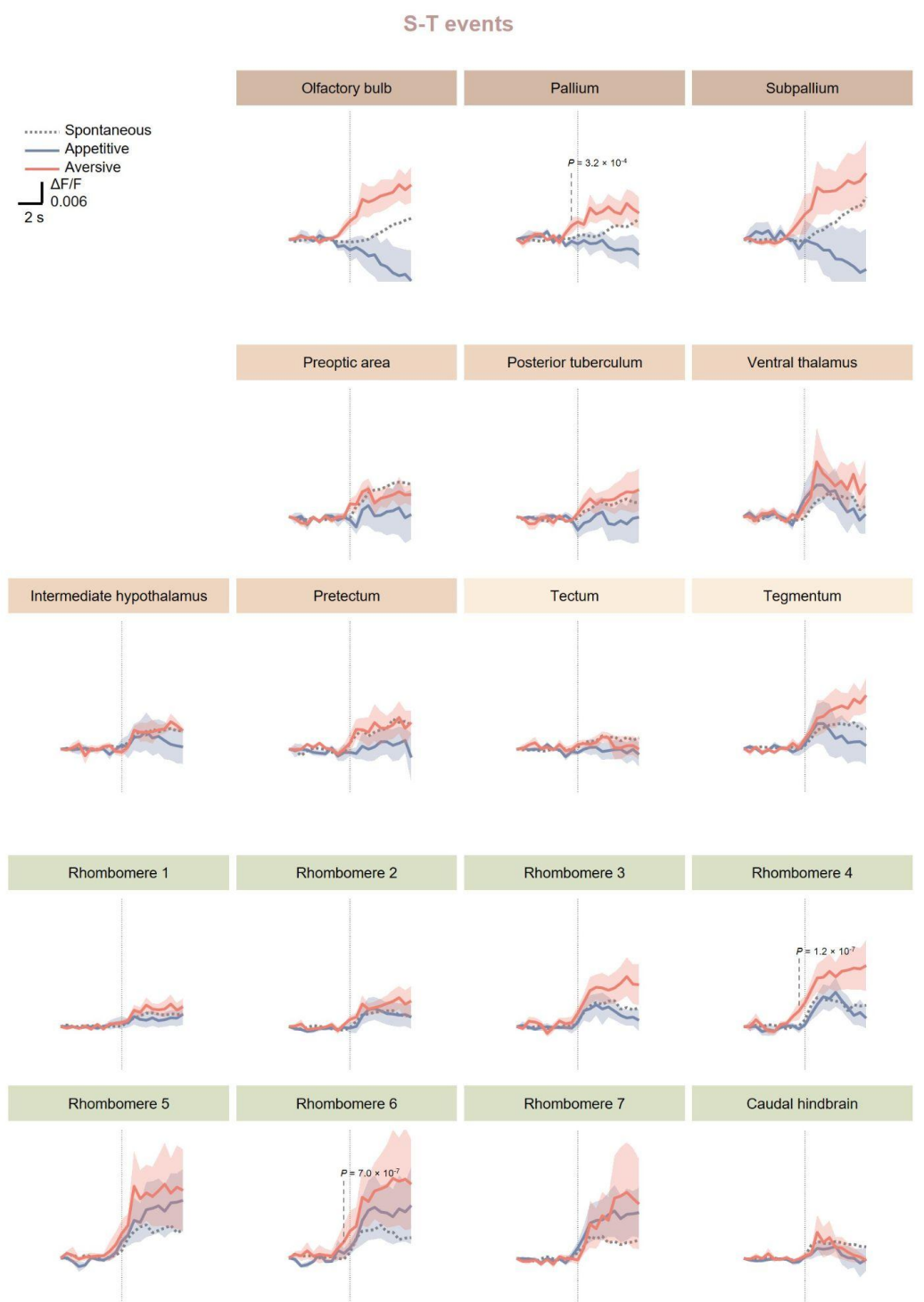
**Supplementary Figure 7. Brain-wide chemical representation.** (a) Mean intensity (to transverse and sagittal planes) of mean mutual information (M.I.) between the calcium signals of appetitive valence-encoding regions-of-interest (ROIs) and the appetitive stimulus regressors ( $(I_{\text{valine}} + I_{\text{alanine}})/2$ , see **Methods**). (b) Regional mean  $\pm$  S.E.M. (across larvae) of mean appetitive M.I. ( $(I_{\text{valine}} + I_{\text{alanine}})/2$ ).  $P$ -value: Two-sided  $t$ -test comparing the pallium and the subpallium. (c) & (d) Similar to (a) & (b) but for mean aversive chemical M.I. ( $(I_{\text{cadaverine}} + I_{\text{putrescine}})/2$ ) and aversive valence-encoding ROIs. (e) Mean intensity projections (to transverse and sagittal planes) of M.I. between the calcium signals of 1 mM valine-encoding ROIs and the stimulus regressor ( $I_{\text{valine}}$ , see **Methods**). (f) Regional mean  $\pm$  S.E.M. (across larvae) of sensory M.I. (g)–(l) Similar to (e) & (f) but for (g) & (h) alanine ( $I_{\text{alanine}}$ ), (i) & (j) cadaverine ( $I_{\text{cadaverine}}$ ) and (k) & (l) putrescine ( $I_{\text{putrescine}}$ ), all at 1 mM. The major brain regions (telencephalon, diencephalon, mesencephalon and rhombencephalon) are color-coded. Abbreviations of brain regions: Same as in **Figure 5b**. In all plots, data are pooled from  $n = 5$  larvae. Scale bars: 50  $\mu\text{m}$  in the Z-Brain Atlas space.

## Supplementary Figure 8



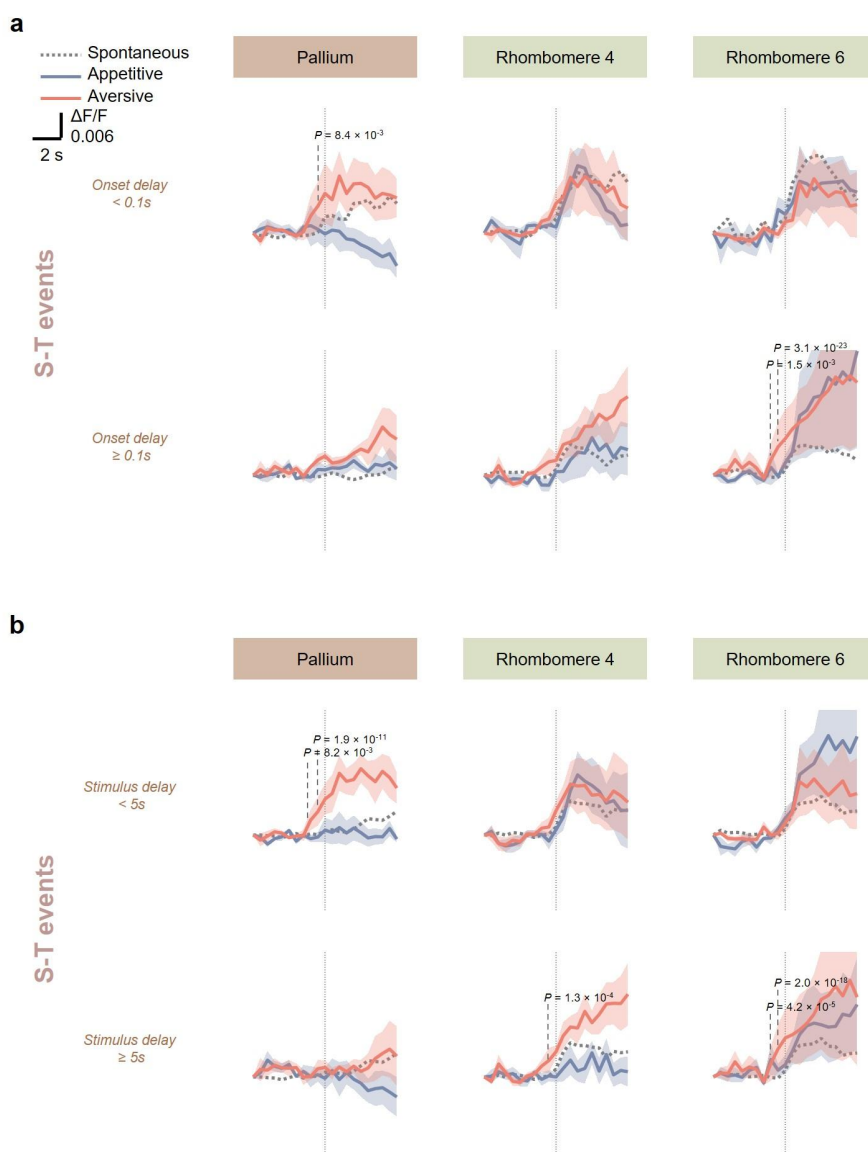
**Supplementary Figure 8. Additional analysis on sensorimotor representations.** (a) Scatter plot of valence preference vs. motor preference of the union set of motor- and valence-encoding neurons. The four quadrants classify neurons into different sensorimotor tuning properties. The neuron sets in Q1 and Q3 are those shown in **Figures 5g, h** and **Figures 5i, j**, respectively. (b) & (c) Zoom-in maps showing the forebrain regions olfactory bulb, pallium and subpallium regions-of-interest (ROIs) preferring (b) S-T event and aversive valence in **Figure 5g**, and (c) independent tail flip and appetitive valence in **Figure 5i**. Scale bars: 50  $\mu$ m in the Z-Brain Atlas space.

## Supplementary Figure 9



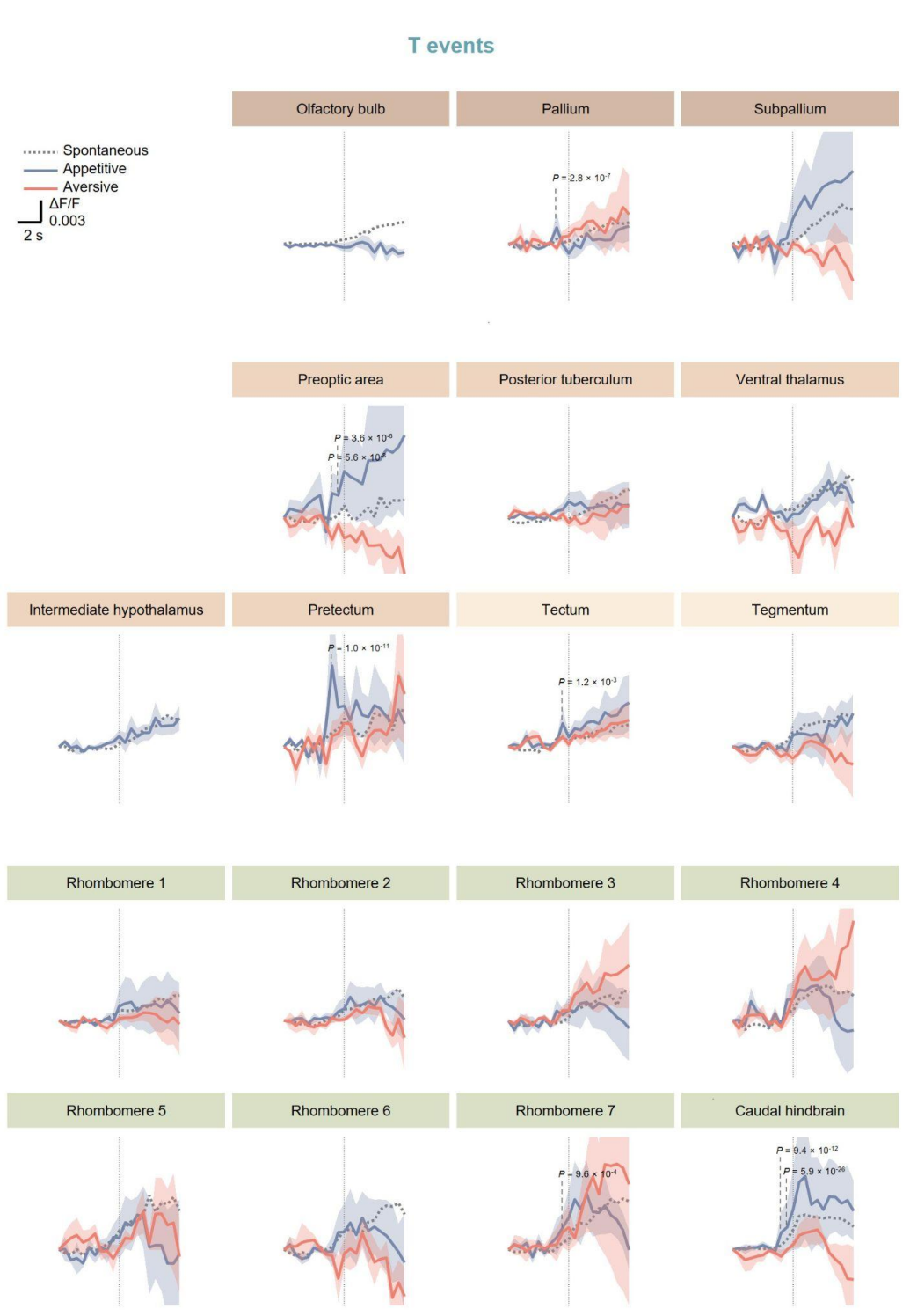
**Supplementary Figure 9. Neuronal activity associated with chemosensory-driven coupled saccade-tail flip (S-T) events across different brain regions.** Mean  $\pm$  S.E.M. (across  $n = 5$  larvae) responses of motor-encoding regions-of-interest (ROIs) in the different brain regions, aligned to the onset of chemosensory cue-associated S-T events. Dotted traces show the corresponding neuronal responses of spontaneous S-T events. Dotted vertical lines indicate tail flip onsets (in a corresponding neuronal imaging frame).  $P$ -values: Right-sided Z-tests comparing pre-chemical cue-associated event neuronal activity at each time point to zero. Significance was set at 2.5 standard deviations (S.D.), with S.D. estimated from spontaneous event baseline activity variability. Adjustment for multiple comparisons across time points and brain regions was made using the Benjamini-Hochberg procedure.

## Supplementary Figure 10



**Supplementary Figure 10. Additional analysis on neural activity underlying chemosensory-driven coupled saccade-tail flip (S-T) events.** Mean  $\pm$  S.E.M. (across  $n = 5$  larvae) responses of motor-encoding regions-of-interest (ROIs) in the pallium, rhombomere 4 and rhombomere 6, classified according to **(a)** saccade-tail flip onset delay [ $< 0.1$  seconds (upper) or  $\geq 0.1$  seconds (lower)] and **(b)** stimulus-tail flip delay [ $< 5$  seconds (upper) or  $\geq 5$  seconds (lower)], and aligned to the onset of chemosensory cue-associated S-T events. Dotted traces show the corresponding neuronal responses of spontaneous S-T events (note that in **(b)**, spontaneous S-T events were not classified according to stimulus-tail flip delay). Dotted vertical lines indicate tail flip onsets (in a corresponding neuronal imaging frame).  $P$ -values: Right-sided Z-tests comparing pre-chemical cue-associated event neuronal activity at each time point to zero. Significance was set at 2.5 standard deviations (S.D.), with S.D. estimated from spontaneous event baseline activity variability. Adjustment for multiple comparisons across time points and brain regions was made using the Benjamini-Hochberg procedure.

## Supplementary Figure 11



**Supplementary Figure 11. Neuronal activity associated with chemosensory-driven independent tail flips (T events) across brain regions.** Mean  $\pm$  S.E.M. (across  $n = 5$  larvae) responses of motor-encoding regions-of-interest (ROIs) in the different brain regions, aligned to the onset of independent tail flips during chemical cue presentation. Dotted traces show the corresponding neuronal responses of spontaneous independent tail flips. Dotted vertical lines indicate tail flip onsets (in a corresponding neuronal imaging frame).  $P$ -values: Right-sided Z-tests comparing pre-chemical cue-associated event neuronal activity at each time point to zero. Significance was set at 2.5 standard deviations (S.D.), with S.D. estimated from spontaneous event baseline activity variability. Adjustment for multiple comparisons across time points and brain regions was made using the Benjamini-Hochberg procedure.